Buoyancy and localizing properties of continental mantle lithosphere: Insights from thermomechanical models of the eastern Gulf of Aden

Louise Watremez, Evgenii E.B. Burov, Elia d'Acremont, Sylvie Leroy, Benjamin Huet, Laetitia Le Pourhiet, Nicolas Bellahsen

Buoyancy and localizing properties of continental mantle lithosphere: Insights from thermomechanical models of the eastern Gulf of Aden

L. Watremez,[1,2,3] E. Burov,[2,3] E. d'Acremont,[2,3] S. Leroy,[2,3] B. Huet,[4] L. Le Pourhiet,[2,3] and N. Bellahsen[2,3]

Corresponding author: L. Watremez, Department of Oceanography, Dalhousie University, Halifax, NS B3H 4R2, Canada. (louise.watremez@dal.ca)

[1]Department of Oceanography, Dalhousie University, Halifax, NS, Canada

[2]ISTeP, UPMC University Paris 06 - UMR 7193, Paris, France

[3]ISTeP, CNRS UMR 7193, Paris, France

[4]Department for Geodynamics and Sedimentology, University of Vienna, A-1090 Vienna, Austria

Abstract. Physical properties of the mantle lithosphere have a strong influence on the rifting processes and rifted structures. In particular, in context of rifting, two of these properties have been overlooked: (1) Mohr-Coulomb plasticity (localizing pressure-dependent) may not be valid at mantle depths as opposed to non-localizing pressure-independent plasticity (hereafter, perfect plasticity), and (2) lithosphere buoyancy can vary, depending on the petrological composition of the mantle. Focussing on the Arabian plate, we show that the lithosphere may be negatively buoyant. We use thermomechanical modeling to investigate the importance of mantle rheology and composition on the formation of a passive margin, ocean-continent transition (OCT) and oceanic basin. We compare the results of this parametric study to observations in the eastern Gulf of Aden (heat-flow, refraction seismics and topography) and show that (1) mantle lithosphere rheology controls the margin geometry and timing of the rifting; (2) lithosphere buoyancy has a large impact on the seafloor depth and the timing of partial melting; and (3) a perfectly plastic mantle lithosphere 20 kg m^{-3} denser than the asthenosphere best fits with observed elevation in the Gulf of Aden. Finally, thermomechanical models suggest that partial melting can occur in the mantle during the Arabian crustal break-up. We postulate that the produced melt could then infiltrate through the remnant continental mantle lithosphere, reach the surface and generate oceanic crust. This is in agreement with the observed narrow OCT composed of exhumed continental mantle intruded by volcanic rocks in the eastern Gulf of Aden.

1. Introduction

Whether or not a large amount of magmatic activity occurs during rifting has led to two separate classes of rifted passive margins: volcanic or non-volcanic margins. Volcanic margins are commonly associated with high thermal anomalies in the mantle, which are often due to mantle plumes like the Afar Plume in the western Gulf of Aden [e.g. *Courtillot et al.*, 1999] or the Islandic Plume in Greenland and Norway [e.g. *Eldholm and Grue*, 1994]. These are characterized by basalt flows (seaward dipping reflectors), volcanoes, and mafic underplating produced during the rifting process [e.g. *Mutter et al.*, 1982; *White and McKenzie*, 1989; *Geoffroy*, 2005]. These margins present a sharp ocean-continent boundary or a very narrow ocean continent transition zone [OCT, e.g. *Bauer et al.*, 2000; *Mjelde et al.*, 2007].

Non-volcanic rifted margins are usually compared to the Iberia margin and are characterized by (1) tectonized features (tilted blocks) and a well identified transitional zone between the continental crust and the oceanic crust, the OCT [e.g. *Whitmarsh et al.*, 1991; *Louden et al.*, 1997; *Lavier and Manatschal*, 2006], or (2) a wide zone of hyper-extended crust [e.g. *Contrucci et al.*, 2004; *Unternehr et al.*, 2010]. Non-volcanic margins actually contain a limited amount of magmatism and there is now a general agreement on describing them as magma-poor margin. The nature of the OCT varies along magma-poor margins [e.g. *Leroy et al.*, 2010a; *Gerlings et al.*, 2011]. It is usually either made of (1) a Zone of Exhumed Continental Mantle [Z.E.C.M., e.g. *Manatschal*, 2004], (2) deeper mantle serpentinized by percolation of the seawater through the sediments and faulted crust [e.g. *Boillot et al.*, 1987; *Pérez-Gussinyé and Reston*, 2001], or (3) highly tectonized oceanic

crust formed by ultra-slow spreading [e.g. *Srivastava and Roest*, 1995; *Sibuet et al.*, 2007]. Another type of magma-poor margin, like the Angolan margin, shows hyper-extended continental crust and evidence of shallow sediments deposition ('sag' basins) during the late phase of rifting [e.g. *Moulin et al.*, 2005].

The factors that control the amount of melt produced at magma-poor margins, either by decompressional melting during crustal thinning [e.g. *Minshull*, 2002] or post-rift thermal anomaly [e.g. *Lucazeau et al.*, 2009], are yet to be understood. Especially, it is still not always clear how the properties of the mantle lithosphere affect the rift evolution and the production of melt, i.e. the nature – volcanic or not – of the margin.

To answer these types of questions, several studies have shown that comparing mechanical models of rifted margin formation to data and field observations is an effective approach [e.g. *Brun and Beslier*, 1996; *Lavier and Manatschal*, 2006; *Huismans and Beaumont*, 2011]. In particular, *Huismans and Beaumont* [2011] show the importance of a viscous lower crust on the necking of the mantle lithosphere and the geometry of Angolan-type magma-poor margins. The eastern Gulf of Aden has been chosen to tackle the problem of Iberia-type magma-poor margin. Indeed, (1) it is well documented, (2) the conjugate passive margins are known as magma-poor and the width and nature of the OCT vary along the margin [presence of magmatism where the OCT is narrow and exhumed mantle where the OCT is wider, *Leroy et al.*, 2010a], and (3) the oceanic basin is young (oceanic accretion began at least 17.6 Ma ago), so the conjugate margins are easily correlable and numerical modeling of the whole basin is possible.

Thermomechanical modeling has been widely used to study the mechanisms of lithosphere extension and the parameters governing the geometry of rifted structures (e.g.

influence of the extension rate, *Bassi*, 1995; *Van Wijk and Cloetingh*, 2002; *Huismans and Beaumont*, 2003; *Burov*, 2007; or of the thermal structure of the lithosphere, *Chéry et al.*, 1989). However, beyond the thermal state and ductile strength of the lithosphere, the effects of (1) plastic behaviour of the mantle lithosphere and (2) buoyancy of the lithosphere with respect to the underlying asthenosphere, on the structure of passive margins, are not yet well understood. It is indeed questionable whether the standard brittle failure criterion [*Byerlee*, 1978] is applicable to mantle lithosphere [e.g. *Watts and Burov*, 2003; *Bürgmann and Dresen*, 2008; *Burov*, 2011] or if weaker mechanisms must be included. Similarly, it has become standard to include phase transition and realistic composition in the crust [e.g. *Yamato et al.*, 2007; *Gerya et al.*, 2008] to study the dynamic of active margins. However, the effect of petrological composition – and especially the extent of depletion – on the buoyancy of mantle lithosphere during continental extension is rarely taken into account, except to explain post rift subsidence anomalies [*Kaus et al.*, 2005]. This well might be an important parameter for rifts, which affect continental lithosphere, such as the Rio Grande rift [*Van Wijk et al.*, 2008], the Baikal rift [*Petit and Déverchère*, 2006], or the Gulf of Aden.

In this paper, we therefore explore the effect of two overlooked key parameters on rift evolution: (1) the failure criterion acting in mantle lithosphere and (2) the buoyancy of the lithosphere. Then, we compare the results of this parametric study to the heat-flow measurements and wide-angle seismic models at the northern margin, and elevation data across the eastern Gulf of Aden. This allows us to better understand how these two parameters influence the presence of magmatism at the OCT together with the nature and width of the OCT.

2. Geodynamic settings

The Arabian plate shows a complex history, with the accretion of terranes in the Neo-Proterozoic [e.g. *Al Husseini*, 2000], the occurrence of the Oman obduction and continental subduction during late Cretaceous [e.g. *Searle*, 1983; *Agard et al.*, 2010] the rifting episode in the Mesozoic [*Bosence*, 1997]. The formation of the Arabian lithosphere is the result of two major tectonic events [*Al Husseini*, 2000]: the Amar collision (640 – 620 Ma) and the Najd rifting (530 – 570 Ma). The ages of the basement rocks of Socotra (southern margin of the eastern Gulf of Aden) are 600 to 860 Ma [U-Pb dating, *Denele et al.*, 2012]. In our models, we therefore consider an approximate age of the Arabian lithosphere of 700 Ma, defining it as a tecton [Neo-Proterozoic lithosphere, e.g. *Griffin et al.*, 2003].

The current Gulf of Aden is a young oceanic basin, which separates Arabia from Somalia, accommodating the difference between their plate velocities (Fig. 1). In absolute motion, both plates move to the north. However, the Arabian plate is faster than the Somalian plate [*Vigny et al.*, 2006]. The difference in velocity leads to a present day opening rate of approximately 2 cm yr^{-1} in the eastern Gulf of Aden [e.g. *Fournier et al.*, 2001]. The rifting of the Arabian-Nubian tecton began ∼34 Ma ago [e.g. *Leroy et al.*, 2012]. Subsequently, seafloor spreading occurred at the latest at 17.6 Ma in the east of the Shukra-el-Sheik Fracture Zone [e.g. *Leroy et al.*, 2004; *d'Acremont et al.*, 2006; *Leroy et al.*, 2012]. A post-rift high thermal regime is observed in the whole Gulf of Aden and is interpreted as being in relation to the Afar hotspot activity [*Lucazeau et al.*, 2009; *Basuyau et al.*, 2010; *Leroy et al.*, 2010b; *Chang and Van der Lee*, 2011].

Studies of dynamic topography show that the doming due to the presence of the Afar hotspot does not influence the topography of the eastern Gulf of Aden [e.g. *Lithgow-*

Bertelloni and Silver, 1998]. Indeed, the eastern Gulf of Aden is roughly 200 km away from the apex of the hotspot. Furthermore, the wavelengths of the structures of the dynamic topography are greater than 4000 km, as they are due to deep mantle sources [e.g. *Hager and Richards*, 1989]. Thus, we do not take the dynamic topography into account in this study.

Tomographic studies show that the Arabian-Nubian lithosphere is approximately 250 km thick [*Ritsema and van Heijst*, 2000; *Debayle et al.*, 2001; *Pasyanos and Nyblade*, 2007]. Receiver functions [*Sandvol et al.*, 1998; *Al Amri*, 1999; *Pasyanos and Walter*, 2002; *Al-Damegh et al.*, 2005; *Tiberi et al.*, 2007; *Al-Hashmi et al.*, 2011; *Al-Lazki et al.*, 2012; *Ahmed et al.*, 2013] and refraction seismic profiles [*Mooney et al.*, 1985] constrain the thickness of the Arabian crust, which varies from 35 km (partly thinned crust, close to the Red Sea and the Gulf of Aden) to 49 km (thickened crust, Oman mountains). We adopt a mean crustal thickness of 44 km for our models, corresponding to the average value of non-thinned and non-thickened Arabian crust. Geophysical studies on the north-eastern Gulf of Aden magma-poor margin show that the OCT is narrow (15 km to 50 km) and presents strong along-margin variations with serpentinization and little volcanism [*Lucazeau et al.*, 2008, 2009, 2010; *Autin et al.*, 2010; *Leroy et al.*, 2010a; *Watremez et al.*, 2011a].

This information will be used both to constrain the initial and boundary conditions of the thermomechanical models presented in section 3 and to compare them with the present structures of the Gulf of Aden. In the parametric study presented here, the aim of the modeling is to better understand the mechanisms of margin formation, such as the north-eastern Gulf of Aden, as well as the nature of their OCT.

3. Parametrization and modeling

3.1. Mantle lithosphere plasticity

The Byerlee [1978] failure criterion is commonly used to represent the yield strength behaviour of rocks. Byerlee's law is written in terms of principal stresses. Hence, it may account for pore-fluid pressure or any other deviations from lithostatic pressure. Extrapolating Byerlee's law at pressures corresponding to depths greater than 40 km implies unrealistically high yield strength for the lithosphere (up to several GPa). Thus, it may not be applicable to the mantle lithosphere [e.g. *Watts and Burov*, 2003; *Précigout et al.*, 2007; *Burov*, 2011]. At this confining pressure, other mechanisms may limit the strength of rocks, including compaction bands, grain boundary sliding [GBS, e.g. *Précigout et al.*, 2007] and Peierls creep [high stress creep for stresses $> 10^3$ MPa, *Kameyama et al.*, 1999]. All these mechanisms limit the strength of the lithosphere at high deviatoric stresses by reducing the pressure dependance of the strength, and decreasing the ability of the lithosphere to localize strain at high strain-rate (except GBS). Furthermore, field observations of exhumed mantle shear zones show strain localization at all scales and no brittle deformation [see a review in *Précigout et al.*, 2007; *Bürgmann and Dresen*, 2008]. In contrast, geophysical imaging of active strike slip faults in the mantle suggests that they are broad (>10-100 km wide) zones of distributed shearing [*Molnar et al.*, 1999; *Little et al.*, 2002; *Sol et al.*, 2007]. There is obviously a scale effect in this apparent contradiction.

To model the brittle-ductile behaviour of rocks, one can use visco-elasto-plastic rheologies based on Maxwell summation for deviatoric strain-rate ($\dot{\epsilon}^d$):

$$\dot{\epsilon}^d = \dot{\epsilon}^d_{vis} + \dot{\epsilon}^d_{elas} + \dot{\epsilon}^d_{plas} \quad (1)$$

The viscous part ($\dot{\epsilon}^d_{vis}$) corresponds to the ductile behaviour of rocks and accounts for deformation by creep. The elastic strain rate ($\dot{\epsilon}^d_{elas}$) is very small but is needed to model the path dependance of the rheology. Finally, the brittle part ($\dot{\epsilon}^d_{plas}$) uses a plastic flow rule to limit the maximal rock strength when a brittle failure criterion is reached. For Byerlee behaviour, the plastic flow rule follows the *Vermeer* [1990] Mohr-Coulomb plastic model, but is limited to an incompressible flow (zero dilatation).

At high confining pressure, Byerlee's law [1978] shows that maximal brittle strength is proportional to 0.6 P, where P is the total pressure. Within our formulation, we model this experimental law using the cohesion $C_0 = 20$ MPa and the internal friction angle $\phi = 30°$. If ϕ is not equal to zero, this results in strain localization (shear banding) due to the apparent strain weakening behaviour [*Vermeer*, 1990; *Le Pourhiet*, 2013]. Mechanisms such as Peierls [for lithospheric extension, e.g. *Popov and Sobolev*, 2008] and GBS [e.g. *Précigout et al.*, 2007] creeps are shown to limit rock strength to 400 to 700 MPa [*Burov*, 2011] and to be weakly pressure dependent. Using the creep parameters of *Hirth and Kohlstedt* [2003] and considering the mean strain rate in the rift area of 10^{-14} s^{-1}, a mantle temperature of 650°C, corresponding to depths of approximately 100 km and an average grain size of 100 μm, the value of the GBS yield stress is approximately 400-500 MPa. Thus, we roughly approximated these mechanisms with $C_0 = 450$ MPa and $\phi = 0°$. As a result, the lithosphere behaves as a perfectly plastic material and no significant localization, without an additional softening law, is predicted to occur. This mechanism is also known as "stress limiter" [*van Hunen et al.*, 2002].

Thus, while Byerlee's parameters predict a large strength peak at ∼90 km depth (more than 1 GPa), the maximal strength in the perfectly plastic mantle lithosphere is constant and limited to a much smaller value (in this study, 450 MPa) for the whole depth interval in the mantle lithosphere, up to 100 km depth (Fig. 2).

3.2. Lithosphere buoyancy

In order to get direct information on the buoyancy of the Arabian mantle lithosphere, density profiles have been calculated for the chemical compositions of Arabian plate mantle xenoliths available in the literature. These calculations have been carried out using the free energy minimization thermodynamic code PERPLEX07 [*Connolly*, 2009], together with a recent thermodynamic database and activity models developed for mantle pressure and temperature conditions and compositions [*Xu et al.*, 2008]. Four average compositions of tecton subcontinental mantle lithosphere [*Griffin et al.*, 2009] were also considered as standard compositions for lithospheres having similar age as the Arabian plate. Since the composition of the asthenosphere below the Arabian plate is unknown, we used the fertile Hawaiian pyrolite composition [*Wallace and Green*, 1991]. This standard is used as a proxy for the density of the asthenosphere influenced by the Afar hot-spot. The buoyancy is calculated as the density difference between asthenosphere and mantle lithosphere: $\rho_{asth} - \rho_{lith}$. The dataset of chemical compositions, the description of the method and the density curves are presented in the Supplementary material.

The chemical composition of the xenoliths and the standards are plotted in a Mg# vs. $\%Al_2O_3$ diagram (Fig. 3A). The xenoliths from the Arabian plate are divided into two chemical groups. The depleted group (lherzolites and harzburgites) plot in the depleted part of the tecton xenoliths (dotted red zone on Fig. 3A). The corresponding compositions

are also more depleted than the tecton and asthenosphere standards. The fertile group (clinopyroxenites and websterites) shows greater scatter.

The clinopyroxenites and websterites are partly [*Henjes-Kunst et al.*, 1990] or entirely [*Stein et al.*, 1993] interpreted as cumulates formed in Pan-African times. These authors do not explicitly specify the geodynamic context for the formation of these rocks. Comparison with modern magmatic arcs [e.g. *Saleeby et al.*, 2003] suggests that they formed as cumulates below arcs, which is consistent with the accretion of the Arabian shield during the end of the Pan-African orogeny [*Frisch and Al-Shanti*, 1977; *Hargrove et al.*, 2006]. These rocks could also correspond to recycled subducted oceanic crust that has been incorporated into the lithosphere during cooling of the mantle [*Hofmann and White*, 1982]. Amounts of recycled oceanic crust in the asthenosphere range mainly between 10% and 20% and reach up to 30% [*Sobolev et al.*, 2007].

The calculated depth profiles of buoyancy are presented in Fig. 3B. Chemical variations are directly reflected by the buoyancy. The more depleted is the composition (low % of Al_2O_3 and high Mg#), the greater is the buoyancy. Lherzolites and harzburgites are buoyant or have a slightly negative buoyancy, whereas all clinopyroxenites and the websterites have a very negative buoyancy. Mean buoyancies averaged over the lithosphere are approximately 20 kg m^{-3} for the lherzolite-harburgite group, -100 kg m^{-3} for the clinopyroxenite-websterite group and 5 kg m^{-3} for the tecton standards.

The Arabian plate mantle lithosphere is a mixing of depleted and fertile rocks, both groups having different buoyancies. The buoyancy of the whole lithosphere can therefore be estimated by a weighted average of the buoyancy of these two end-members. In order to take into account the complex history of the Arabian plate, we propose two models

(Fig. 3C). In the first model, the depletion of lherzolites and harzburgites is inherited from partial melting coeval with the formation of the Arabian shield [*Stein et al.*, 1993]. The depleted end-member corresponds to the mean of the lherzolite-harzburgite group. The fertile end-member corresponds to the mean of the clinopyroxenite-websterite group (blue line on 3C). A mantle lithosphere composed of 35% clinopyroxenite-websterite and 65% lherzolite-harzburgite has a negative buoyancy of ∼20 kg m^{-3}. In the second model, the depletion is due to Miocene partial melting that postdates the onset of rifting [*McGuire*, 1988]. The depleted end-member is the mean of the tecton standards and the fertile end-member corresponds to the mean of the clinopyroxenite-websterite group (red line on 3C). 25% clinopyroxenite-websterite is sufficient to explain a negative buoyancy of ∼20 kg m^{-3}. A few 10s kg m^{-3} negative buoyancy can therefore be explained by a significant proportion (∼30%) of heavy clinopyroxenite and websterite. Using a different asthenosphere composition indicates a difference of ∼10 kg m^{-3}. Hence, a reduction of the amount of clinopyroxenite and websterite by 15-25% would induce an average buoyancy of -20 kg m^{-3}. In the parametric study, we apply a ±30 kg m^{-3} buoyancy in order to test extreme parameters.

3.3. Parametrization and numerical modeling

We use Flamar 12 [an outgrowth of Paravoz, *Burov and Yamato*, 2008] that is inspired by the FLAC v3 algorithm [*Cundall*, 1989; *Poliakov et al.*, 1993]. The numerical method has been described in full detail in previous studies [e.g. *Burov and Poliakov*, 2001; *Burov and Cloetingh*, 2009; *François et al.*, in press]. This method can handle a free upper surface boundary condition and almost any visco-elasto-plastic rheology. The algorithm explicitly takes into account elastic-brittle-ductile properties of lithosphere and asthenosphere. Due

to the explicit nature of this code for elastic compressibility, temperature, gravity and pressure-dependent body forces are computed without the necessity to use assumptions such as potential temperature. The description is limited here to the details that are the most essential for this study.

Our model setup is inspired by previous rifting models achieved with the same numerical thermomechanical code [*Burov*, 2007, Fig 2]. The modeling box is 400 km thick and 1200 km wide; grid resolution is 4 km in both directions. The properties of each element of the numerical grid (cell) are defined by the density and the thermal and elasto-visco-plastic parameters of its material. We use a density and rheology structure from the lithosphere and asthenosphere derived from *Ranalli* [1995]. All models include a 44 km thick crust with four horizontal rheological layers. The parameters of the reference model are presented in Table 1. Materials in the specific numerical formulation used for the study are elasto-visco-plastic. To avoid activation of Mohr-Coulomb plastic deformation in the asthenosphere [which is unlikely, e.g. *Watts and Burov*, 2003], we assigned high cohesion values to the asthenosphere.

The boundary conditions are (1) horizontal extension velocities (V_{ext}) applied at each vertical side of the model, (2) a Winckler pliable basement that simulates the response to lithostatic pressure variations and (3) a free upper surface boundary condition (free stress and free slip conditions in all directions) combined with a moderate diffusion erosion and sedimentation ($k_{eros} = 50$ m^2 yr^{-1}) and water-column pressure dependent on the surface topography (Fig. 2). The elevation at each point of the free surface is calculated following the model of *Culling* [1960], which takes into account the effect of erosion and sedimentation.

The assumed initial thermal structure is constrained by the radiogenic heat production in the crust, the age the lithosphere and the temperature at the base of the lithosphere. It is noteworthy that, after 600 Ma, the thermal structure of thermally undisturbed lithosphere reaches a permanent state. Thus, there is no practical difference in the thermal structure of a 600 Ma or, for example, a 2000 Ma old lithosphere [e.g. *Burov and Diament*, 1995]. The thermal age in the models is 700 Ma, to be consistent with the real age of the Arabian shield.

The main parameters tested in this study are the plastic failure pressure dependence and the buoyancy of the mantle lithosphere.

3.4. Areas of possible partial melting

Partial melting is not supposed to have a strong impact on the overall rift evolution of the Eastern Gulf of Aden, as its rifted margins are magma-poor. The lack of a small production of melt at break-up is therefore a non-negligible constraint on the validity of the models. Some codes include partial melting in the modeling, in order to simulate mantle convection [e.g. *ONeill et al.*, 2006]. However, for the sake of simplicity, it is not necessary to directly include partial melting calculations. We follow the simplified approach developed by *McKenzie and Bickle* [1988], which consists in calculating the areas where partial melting can occur. We compute the location of these areas at the post-processing stage. The method uses the model-predicted pressure and temperature conditions in the mantle as input, and output a melt fraction. We consider the areas where the melt fraction [defined in *McKenzie and Bickle*, 1988] is between 0 and 1. This post-processing allows us to assess whether melt can be produced during the rifting and to characterize the nature of the OCT in the model.

4. Parametric study

4.1. Influence of mantle lithosphere rheology

Figure 4 compares two models with different mantle rheology and highlights the influence of this parameter on rifting evolution and rifted margins formation.

As expected from the rheology law, deformation is more diffuse in the perfectly plastic mantle than in a Byerlee's mantle. Meanwhile, strain localization is also enhanced by the higher strength of a Byerlee's lithosphere and the imposed velocity boundary condition. This lack of localization results in delaying the break-up of continental crust by 1.5 Myr for the model with the perfectly plastic mantle. As the strain localization is more intense in the Mohr-Coulomb mantle lithosphere, deformation propagates faster through the continental crust. Moreover, the strain rate patterns 0.5 Ma before the break-up of the continental crust show an asymmetric deformation in the upper mantle beneath the continental rift for the Mohr-Coulomb model, while the perfectly plastic model remains symmetric (Fig. 4A).

Crustal flexure (shape of the continental crust aside the rift) – and hence flexural stresses – at the time of crustal break-up is more intense for the Mohr-Coulomb model than for the perfectly plastic model, contributing to an earlier break-up for the former (Fig. 4A). As can be seen the local extrema of topography coincide in either case, producing close values of flexural wavelength (∼250 km) and, hence, of elastic thickness (Fig. 4B). The corresponding equivalent flexural thickness estimated using analytical formulae for the flexural parameter [*Turcotte and Schubert*, 2002] is on the order of 40 km. This wavelength is largely controlled by the strongest part of the mantle lithosphere [*Burov and Diament*, 1995]. The difference in amplitude at rift flanks refers to smaller levels of flexural stress in

the crust in case of a less localizing, perfectly-plastic rheology. We observe that no partial melting can occur in the mantle lithosphere for either model, suggesting that continental mantle can be exhumed without production of oceanic crust in either case.

In order to compare the models with the present day Gulf of Aden, we compare their geometries and bathymetries 18 Ma after break-up. The geometry of the structures at this moment also shows a slightly stronger flexure for the Mohr-Coulomb model than for the perfectly plastic model, while conjugate margins are still asymmetric (Fig. 4A). The slope of the Moho discontinuity is also steeper for the Mohr-Coulomb model than for the perfectly plastic model, implying a wider distal margin with the perfectly plastic configuration. Moreover, the ridge location shows a strong asymmetry in the Mohr-Coulomb model, contrary to the perfectly plastic model. This can be attributed to the fact that a Mohr-Coulomb mantle localizes the deformation better, allowing for further strain to occur on the fault formed along the margin at the break-up of the continental crust. Comparison of the topography 18 Ma after continental crust break-up provides a similar amplitude of the topography for both models, but the same asymmetry is recovered as the oceanic ridge is highlighted by a deeper zone along the model (Fig. 4B). We also observe the development of this asymmetry on the evolution of the topography (distance versus time, Fig. 4C). Indeed, after continental break-up, the ridge tends to be localized close to the margin during approximately 10-12 Myr for the Mohr-Coulomb model. The ridge remains stable until the fault zone reaches a hardening sufficient to cause a relocation of the ridge. On the contrary, the ridge in the perfectly plastic model is centered from the onset of the formation of the oceanic basin. This difference is due to the fact that the perfectly plastic mantle has a more diffuse deformation mechanism than the Mohr-

Coulomb mantle. The model with the perfectly plastic mantle also shows an oceanic ridge that is centered in the same way as observed in the Gulf of Aden, giving additional preference to the perfectly plastic model over the Mohr-Coulomb model.

It can be concluded that the choice of the failure criterion in the mantle lithosphere has a significant impact on the extensional deformation in the upper mantle, and indirectly in the continental crust. Compared to the Mohr-Coulomb mantle, the assumption of a perfectly plastic mantle allows for a more diffuse deformation, with the following consequences: (1) more extension is needed to break the crust apart, (2) the flexure is more gentle, and (3) the horizontal position of the oceanic ridge, as observed in the Gulf of Aden, is more consistent with observation. However, oceanic basins predicted by both models are deeper than the observed topography profiles across the Gulf of Aden. Hence, additional factors such as mantle density should be explored to explain the shallowness of the oceanic basin of the Gulf of Aden.

4.2. Influence of lithosphere buoyancy

The three model-setups are identical to the Mohr-Coulomb setup previously presented (Table 1), except for the density of the asthenosphere, in order to test the influence of the buoyancy of the lithosphere on the rifting and the formation of rifted structures (Fig. 5). Thus, we compare three series of experiments with different lithosphere buoyancy (see paragraph 3.2 for definition). The three values of buoyancy tested here are -30, 0 and +30 kg m^{-3}. The model with a positive buoyancy (30 kg m^{-3}) is the same as the Mohr-Coulomb configuration described in paragraph 4.1.

Our first observation is that the variation of the buoyancy of the lithosphere does not affect the timing of the break-up of the continental crust. Indeed, this break-up occurs 7 Ma after the beginning of the extension for all three models.

The strain rate patterns 0.5 Ma before the break-up of continental crust show an asymmetry beneath the center of the rift zone for the two models with non-zero buoyancy (Fig. 5A). This is probably due to the fact that the zero lithosphere buoyancy reduces the mechanical contrast between the mantle lithosphere and the asthenosphere, avoiding asymmetric processes to occur at this stage.

The geometry of the models at the moment of the continental crust break-up shows a shallower boundary between mantle lithosphere and asthenosphere, as asthenosphere density is lower than for the other tested models (Fig. 5A). This is simply due to the fact that the lighter the material is, the more rapidly it uplifts. We observe that a zone of possible partial melting occurs at the center of the rift for the model with a negative buoyancy (-30 kg m^{-3}). Indeed, in this model the 1300°C isotherm (approximately the base of the lithosphere) is shallow enough at the time of break-up of the continental crust to allow for partial melting. This implies that oceanic crust can be produced at this time, while magmatism may occur earlier, producing underplated and/or intruded magma, as the continental crust is not yet broken apart. This process is characteristic of the formation of volcanic passive margins.

Model geometries 18 Ma after the break-up of the continental crust show asymmetric margins in all cases. We observe that the lateral position of the oceanic ridge is more centered when buoyancy is negative (Fig. 5A-B, see also topographic profiles). Indeed, predicted evolution of the topography shows that the oceanic ridge relocates after 10-

12 Ma for the model with positive buoyancy and after 6-7 Ma for the model with zero buoyancy. The model with negative buoyancy shows an early relocation at the beginning of the formation of the oceanic basin (Fig. 5C). We also observe that the depth of the oceanic basin increases when asthenosphere is denser, which is consistent with the isostasy effect, and that the model with a negative lithosphere buoyancy provides a better fit to the present depth of the Gulf of Aden oceanic basin.

Thus, the buoyancy of the lithosphere controls (1) the depth of the oceanic basin, (2) the position and the relocation of the oceanic ridge in the basin, and (3) the volcanic or magma-poor nature of the rifted margins. A negative buoyancy of the lithosphere allows for a depth of the oceanic basin comparable with observations in the eastern Gulf of Aden.

5. Discussion

5.1. Comparison to the eastern Gulf of Aden

The choice of parameters for this model is governed by the results of the parametric study (failure criterion in the mantle lithosphere and buoyancy of the lithosphere) and the geodynamic context (kinematics). Thus, we use a perfectly plastic mantle and a negative lithosphere buoyancy of -20 kg m^{-3}, which is petrologically more realistic than the value of -30 kg m^{-3} used in the parametric study. Then, we modify the boundary conditions to better fit the actual kinematics (see Section 2): a velocity of 0.5 cm yr^{-1} is applied on the left side (South), while a velocity of 1.5 cm yr^{-1} is applied on the right side (North), to keep a total opening velocity of 2 cm yr^{-1}. The small initial thermal anomaly used to localize the rift is set closer to the left side of the box, to ensure that the rift is at the center of the box at the final stage (18 Ma after crustal break-up), comparable to the present-day Gulf of Aden.

We compare the model at 18 Ma after the break-up of the continental crust to the data available at the same scale in the eastern Gulf of Aden (Fig. 6). First, heat-flow at the surface of the model is similar to heat-flow measurements for large wave-lengths on the northern margin [Fig. 6A, *Lucazeau et al.*, 2008]. Next, geometry of the crustal thinning is comparable with refraction and wide-angle reflection seismic velocity model along the same line [Fig. 6B, *Leroy et al.*, 2010a]. However, the crude resolution of the model does not allow for a more detailed match with the observed structures in the sediments and crust. Finally, the topography of the model shows the same amplitude as profiles across the eastern Gulf of Aden, even though the morphology of the rift shoulders is steeper than the observation (Fig. 6C). The oceanic basin is also slightly deeper in the model than in the data. In the eastern Gulf of Aden, higher than expected mantle heat-flow and lower than expected seismic velocity and density values, inferred from wide-angle seismic and gravity modeling, might be explained by a persistent post-rift thermal anomaly [*Lucazeau et al.*, 2008; *Watremez et al.*, 2011a]. This topographic discrepancy might be explained by the high thermal regime affecting the entire Gulf [e.g. *Lucazeau et al.*, 2008, 2009, 2010; *d'Acremont et al.*, 2010; *Leroy et al.*, 2010b].

We also observe that pressure and temperature conditions in the asthenosphere at the center of the rift allow for partial melting at the exact moment of the break-up of the continental crust (Fig. 6B). The melt produced can infiltrate toward the surface and either (1) become trapped beneath the margin (underplating, magmatism) to form a volcanic margin and/or (2) generate oceanic crust, leaving very little time to serpentinize or exhume continental mantle, forming a magma-poor margin. This is consistent with the north-eastern Gulf of Aden margin that exhibits a very narrow OCT and even some

magmatism [*Autin et al.*, 2010; *Leroy et al.*, 2010a; *Watremez et al.*, 2011a; *Leroy et al.*, 2012], which may have triggered the continental break-up, as shown by *Bronner et al.* [2011] for the Iberia margin.

5.2. Perfectly plastic failure criterion

The parametric study shows that a perfectly plastic mantle lithosphere allows for stronger ridge relocation than a Mohr-Coulomb lithosphere, resulting in a ridge topography more comparable to the present Gulf of Aden morphology.

The choice of the failure criterion in the mantle governs the deformation in the mantle lithosphere and then the deformation in the continental crust. The perfectly plastic criterion makes deformation more diffuse in the lithosphere, while deformation is more localized with the Mohr-Coulomb mantle (narrower shear zones), using the same extension velocity (or strain rate). This explains why the break-up of the continental crust occurs earlier in the case of the Mohr-Coulomb mantle model.

These results are compatible with recent rheological and modeling studies [e.g. *Kameyama et al.*, 1999; *Watts and Burov*, 2003; *Popov and Sobolev*, 2008], which propose that a Mohr-Coulomb rheology (in the form of Byerlee's frictional plastic law) is less suitable for localized deformation of rocks in a high stress regime, especially in extension, than Peierls or GBS rheologies. An alternative model advances the potential role of diking that is supposed to weaken the lithosphere prior to rifting [e.g. *Buck*, 2004]. However, pre-rift diking would lead to extensive pre-rift magmatism and formation of volcanic margins, excluding the possibility to form a magma-poor rifted margin such as the eastern Gulf of Aden.

5.3. Negative buoyancy of the continental lithosphere

The parametric study shows that the buoyancy of the mantle lithosphere has a strong influence on the volcanic or magma-poor nature of the modeled rifted margin. Indeed, a highly negatively buoyant mantle lithosphere (-30 kg m^{-3}) leads to the formation of melt in the asthenosphere prior to crustal breakup, as observed along volcanic margins. On the contrary, a greater buoyancy leads to the formation of typical magma-poor margins, with a zone of exhumed continental mantle.

The comparison between observed and modeled Gulf of Aden topography suggests that the mantle lithosphere of the Arabian shield has a negative buoyancy of approximately -20 kg m^{-3}. Such values have also been proposed for the Baikal rift [*Gao et al.*, 1994; *Petit and Déverchère*, 2006]. Moreover, thermodynamical modeling of the density for a large mantle rock database has shown that mantle lithosphere of tectons can have slightly negative buoyancy for conductive geotherms [*Griffin et al.*, 2009].

The assumption of a subcontinental lithosphere composition close to lherzolitic leads to a positive buoyancy in the case of the Arabian shield (Fig. 3B), which is not in agreement with the result of the models (Section 4.2). However, the heterogeneity and the complex history of the mantle lithosphere are attested by many studies [*Kuo and Essene*, 1986; *McGuire*, 1988; *Stein et al.*, 1993; *Nasir and Safarjalani*, 2000; *Kaliwoda et al.*, 2007; *Shaw et al.*, 2007].

One can doubt the long-term stability of a continental lithosphere with negative buoyancy with respect to the asthenosphere. In this case, we expect Rayleigh-Taylor instabilities after 300-400 Ma, which lead to the collapse of the continental lithosphere [e.g. *Burov and Watts*, 2006]. However, *Lenardic and Moresi* [1999] show that a positive buoyancy

of the lithosphere is not sufficient to create conditions for its long term stability. This stability also depends on the strength of the lithosphere, an effective coupling between the very buoyant crust and the mantle, as well as the occurrence of compressive stresses [*François et al.*, in press]. The Arabian plate actually experienced such significant compressive stresses due to successive subductions [*Al Husseini*, 2000], potentially explaining why it did not collapse.

Similarly to our work, former observations and numerical models show that a negative lithosphere buoyancy should lead to the development of Rayleigh-Taylor instabilities at the mantle-asthenosphere boundary during the rifting, resulting in removal of an essential amount of lithosphere mantle [e.g. *Burov*, 2007; *Van Wijk et al.*, 2008]. This has a strong influence on the rifted structures.

6. Conclusions

The results of our modeling study show that the structure of the rifted continental margins is highly sensitive to the failure criterion of the mantle lithosphere while the buoyancy of the mantle lithosphere controls the depth of the oceanic basin and the relative timing of the partial melting. The model using a perfectly plastic rheology and negatively buoyant mantle lithosphere (-20 kg m^{-3}) shows similar features as the eastern Gulf of Aden (heat-flow, topography, thinning of the continental crust, narrow OCT and position of the ridge).

The perfectly plastic behavior represents a proxi for low temperature plasticity [e.g. *Kameyama et al.*, 1999] whereas Mohr-Coulomb rheology produces higher stress and stress drop, which best represents brittle behaviour at geodynamic time-scale. In the case of the Gulf of Aden, structures are best fitted with a maximum yield strength of 450 MPa, which

is consistent with laboratory derived low temperature plasticity mecanism such as GBS and Peierls creep [*Kameyama et al.*, 1999; *Précigout et al.*, 2007]. *Popov and Sobolev* [2008] study, based on 3D model of continental rifting, argued that Mohr-Coulomb required unrealistic stress build-up during continental rifting. Here, we reach similar conclusions comparing our continental break-up model to the structures of the Gulf of Aden. Not only, stress build-up is too strong, causing the formation of far too high rift shoulders during continental rifting, but Mohr-Coulomb rheology also induced non realistic post-rift topography and extremely long lasting initial phase of asymmetric spreading (10-12 Myr), which is neither observed in Aden nor anywhere else in world.

The Gulf of Aden represents the tipping point between the formation of (1) volcanic rifted margins, where partial melting possibility occurs before the crustal break-up and oceanic crust is created as soon as the continental crust is broken apart by dikes, and (2) magma-poor rifted margins, where partial melting occurs after crustal break-up and a zone of exhumed continental mantle forms between the last continental crust and the first oceanic crust [e.g. *White and McKenzie*, 1989; *Whitmarsh et al.*, 1991; *Bauer et al.*, 2000]. Our parametric study shows that negatively buoyant lithosphere favors early occurrence of melting, whereas neutrally to positively buoyant mantle lithosphere causes the melting to be delayed by up to 1.5 Myr [*Watremez et al.*, 2011b]. Therefore, we posit that mantle buoyancy variation could control the timing of melting and oceanization observed over a wide range of passive margins. In the case of the Gulf of Aden, the first appearance of partial melting in the rift is synchronous with the crustal break-up, which is shown to correspond to a lithosphere that is negatively buoyant by a contrast of -20 kg m^{-3}. This density contrast is confirmed by the petrological study of xenolith of the Arabian mantle

lithosphere and has also been shown to be a decisive factor for the occurrence of oceanic obduction in North Oman using different boundary condition and numerical approach [*Duretz et al.*, 2013].

This panel of evidences implies that the negatively buoyant mantle lithosphere of the Arabian plate has been stable for several hundreds of million years. It rises the question of the dynamic forces, which could be responsible for the long lasting stability and rapid destabilization of old continental lithosphere at the onset of rifting. Further thermomechanical modeling of rifting, including petrological data to estimate the buoyancy of the lithosphere and comparison to other geological region such as the Rio Grande Rift [*Song and Helmberger*, 2007; *Van Wijk et al.*, 2008], are needed to better constrain the links between partial melting and the rheology and buoyancy of continental mantle lithosphere highlighted by our study.

Acknowledgments. The authors thank A. Popov, an anonymous reviewer and the editor, T. Becker, for highly constructive comments. We also want to thank M. Cannat and R. Huismans for helpful discussions. L.W. is grateful to her supervisors, K. Louden and M. Nedimović, for their support during the preparation of this manuscript. L.W. thanks K. Louden for help with proofreading. B.H. would like to thank T. Ntaflos for the discussion on clinopyroxenites and J. Connolly for his answers concerning PERPLEX. Figure 1 has been produced using the GMT package [*Wessel and Smith*, 1995]. The ANR Rift2Ridge, YOCMAL, CNRS-INSU and Action Marges provided the financial support for this study.

References

Agard, P., M. P. Searle, G. I. Alsop, and B. Dubacq (2010), Crustal stacking and expulsion tectonics during continental subduction: P-T deformation constraints from Oman, *Tectonics*, *29*(5), 19 p.

Ahmed, A., C. Tiberi, S. Leroy, G. Stuart, D. Keir, J. Sholan, K. Khanbari, I. Al-Ganad, and C. Basuyau (2013), Crustal structure of the rifted volcanic margins and uplifted plateau of Western Yemen from receiver function analysis, *Geophys. J. Int*, doi:10.1093/gji/ggt072.

Al Amri, A. M. S. (1999), The crustal and upper-mantle structure of the interior Arabian Platform, *Geophys. J. Int.*, *136*, 421–430.

Al-Damegh, K., E. Sandvol, and M. Barazangi (2005), Crustal structure of the Arabian plate: new constraints from the analysis of teleseismic receiver functions, *Earth Planet. Sci. Lett.*, *231*(3-4), 177–196.

Al-Hashmi, S., R. Gök, K. Al-Toubi, Y. Al-Shijbi, I. El-Hussain, and A. J. Rodgers (2011), Seismic velocity structure at the southern margin of the Arabian Peninsula, *Geophys. J. Int.*, *186*(2), 782–792.

Al Husseini, M. I. (2000), Origin of the Arabian Plate structures; Amar collision and Najd Rift, *GeoArabia*, *5*(4), 527–542.

Al-Lazki, A., C. Ebinger, M. Kendall, G. Hellfrich, S. Leroy, C. Tiberi, G. Stuart, and K. Al-Toubi (2012), Upper mantle anisotropy of southeast Arabia passive margin (Gulf of Aden northern conjugate margin), Oman., *Arab. J. Geosci.*, *5*(5), 925–934, doi: 10.1007/s12517-011-0477-2.

552 Autin, J., S. Leroy, E. d'Acremont, M.-O. Beslier, A. Ribodetti, N. Bellahsen, P. Razin,
553 and C. Robin (2010), Continental break-up history of a deep magma-poor margin from
554 seismic reflection data (northeastern Gulf of Aden margin, offshore Oman), *Geophys.*
555 *J. Int*, *180*, 501–519.

556 Bassi, G. (1995), Relative importance of strain rate and rheology for the mode of conti-
557 nental extension, *Geophys. J. Int*, *122*(1), 195–210.

558 Basuyau, C., C. Tiberi, S. Leroy, G. Stuart, A. I. Al-Lazki, K. Al-Toubi, and C. Ebinger
559 (2010), Evidence of partial melting beneath a continental margin: case of Dhofar, in
560 the Northern Gulf of Aden (Sultanate of Oman), *Geophys. J. Int*, *180*, 520–534.

561 Bauer, K., S. Neben, B. Schreckenberger, R. Emmermann, K. Hinz, N. Fechner, K. Gohl,
562 A. Schulze, R. Trumbull, and K. Weber (2000), Deep structure of the Namibia continen-
563 tal margin as derived from integrated geophysical studies, *J. Geophys. Res.*, *105*(B11),
564 25,829–25,853.

565 Boillot, G., M. Recq, E. Winterer, A. Meyer, J. Applegate, M. Baltuck, J. Bergen, M. Co-
566 mas, T. Davies, K. Dunham, et al. (1987), Tectonic denudation of the upper mantle
567 along passive margins: a model based on drilling results (ODP Leg 103, western Galicia
568 margin, Spain), *Tectonophysics*, *132*(4), 335–342.

569 Bosence, D. (1997), Mesozoic rift basins of Yemen, *Mar. Pet. Geol.*, *14*(6), 611.

570 Bronner, A., D. Sauter, G. Manatschal, G. Péron-Pinvidic, and M. Munschy (2011),
571 Magmatic breakup as an explanation for magnetic anomalies at magma-poor rifted
572 margins, *Nat. Geosci.*, *4*(8), 549–553.

573 Brun, J.-P., and M.-O. Beslier (1996), Mantle exhumation at passive margins, *Earth*
574 *Planet. Sci. Lett.*, *142*(1-2), 161–173.

Buck, W. (2004), Consequences of athenospheric variability on continental rifting, in *Rheology and Deformation of the Lithosphere at continental margins*, vol. 62, edited by G. D. Karner, B. Taylor, N. W. Driscoll, and D. L. Kohlstedt, pp. 1–30, Columbia University Press.

Bürgmann, R., and G. Dresen (2008), Rheology of the lower crust and upper mantle: Evidence from rock mechanics, geodesy, and field observations, *Annu. Rev. Earth Planet. Sci.*, *36*, 531–567.

Burov, E. (2011), Rheology and strength of the lithosphere, *Mar. Pet. Geol.*, *28*(8), 1402–1443.

Burov, E., and M. Diament (1995), The effective elastic thickness (T_e) of continental lithosphere: What does it really mean?, *J. Geophys. Res.*, *100*(B3), 3905–3927.

Burov, E., and P. Yamato (2008), Continental plate collision, PTtz conditions and unstable vs. stable plate dynamics: insights from thermo-mechanical modelling, *Lithos*, *103*(1-2), 178–204.

Burov, E. B. (2007), The role of gravitational instabilities, density structure and extension rate in the evolution of continental margins, *Geol. Soc. Spec. Publ.: Imaging, Mapping and Modelling Continental Lithosphere Extension and Breakup*, *282*, 139–156.

Burov, E. B., and S. A. P. L. Cloetingh (2009), Controls of mantle plumes and lithospheric folding on modes of intra-plate continental tectonics: differences and similarities, *Geophys. J. Int.*, *178*, 1691–1722.

Burov, E. B., and A. Poliakov (2001), Erosion and rheology controls on syn and post-rift evolution: verifying old and new ideas using a fully coupled numerical model., *J. Geophys. Res.*, *106*(B8), 16,461–16,481.

598 Burov, E. B., and A. B. Watts (2006), The long-term strength of continental lithosphere:
599 "jelly-sandwich" or "crème-brûlée"?, *GSA Today*, *16*, 4–10.
600 Byerlee, J. (1978), Friction of rocks, *Pure Appl. Geophys.*, *116*(4), 615–626.
601 Chang, S., and S. Van der Lee (2011), Mantle plumes and associated flow beneath Arabia
602 and East Africa, *Earth Planet. Sci. Lett.*, *302*(3-4), 448–454.
603 Chéry, J., M. Daignières, F. Lucazeau, and J. Vilotte (1989), Strain localization in rift
604 zones (case of a thermally softened lithosphere): a finite element approach, *Bull. Soc.*
605 *Geol. Fr.*, *8*, 437–443.
606 Connolly, J. (2009), The geodynamic equation of state: what and how, *Geochem. Geophys.*
607 *Geosyst.*, *10*, Q10,014.
608 Contrucci, I., L. Matias, M. Moulin, L. Géli, F. Klingelhofer, H. Nouzé, D. Aslanian, J. L.
609 Olivet, J. P. Réhault, and J. C. Sibuet (2004), Deep structure of the West African con-
610 tinental margin (Congo, Zaire, Angola), between 5 S and 8 S, from reflection/refraction
611 seismics and gravity data, *Geophys. J. Int.*, *158*(2), 529–553.
612 Courtillot, V., C. Jaupart, I. Manighetti, P. Tapponnier, and J. Besse (1999), On causal
613 links between flood basalts and continental breakup, *Earth Planet. Sci. Lett.*, *166*(3-4),
614 177–195.
615 Culling, W. (1960), Analytical theory of erosion, *J. Geol.*, *68*, 336–344.
616 Cundall, P. (1989), Numerical experiments on localization in frictional materials, *Arch.*
617 *Appl. Mech.*, *59*(2), 148–159.
618 Debayle, E., J. Léveque, and M. Cara (2001), Seismic evidence for a deeply rooted low-
619 velocity anomaly in the upper mantle beneath the northeastern Afro/Arabian continent,
620 *Earth Planet. Sci. Lett.*, *193*(3-4), 423–436.

Denele, Y., S. Leroy, E. Pelleter, R. Pik, J.-Y. Talbot, and K. Khanbari (2012), The Cryogenian juvenile arc formation and successive high-K calc-alkaline plutons intrusion of Socotra island (Yemen), *Arab. J. Geosci.*, *5*(5), 903–924, doi:10.1007/s12517-011-0476-3.

d'Acremont, E., S. Leroy, M. Maia, P. Patriat, O. Beslier Marie, N. Bellahsen, M. Fournier, and P. Gente (2006), Structure and evolution of the eastern Gulf of Aden; insights from magnetic and gravity data (Encens-Sheba MD117 cruise), *Geophys. J. Int.*, *165*(3), 786–803.

d'Acremont, E., S. Leroy, M. Maia, P. Gente, and J. Autin (2010), Volcanism, jump and propagation on the Sheba Ridge, eastern Gulf of Aden: Segmentation evolution and implications for accretion processes, *Geophys. J. Int.*, *180*, 535–551.

Duretz, T., P. Agard, P. Yamato, T. Gerya, and E. Burov (2013), Obduction at plate boundaries : thermo-mechanical modelling, *Geophys. Res. Abstracts*, *Vol. 15*(33), EGU2013–9724.

Eldholm, O., and K. Grue (1994), North Atlantic volcanic margins: dimensions and production rates, *J. Geophys. Res.*, *99*(B2), 2955–2968.

Farr, T., P. Rosen, E. Caro, R. Crippen, R. Duren, S. Hensley, M. Kobrick, M. Paller, E. Rodriguez, L. Roth, et al. (2007), The shuttle radar topography mission, *Rev. Geophys.*, *45*(2), 33.

Fournier, M., P. Patriat, and S. Leroy (2001), Reappraisal of the Arabia–India–Somalia triple junction kinematics, *Earth Planet. Sci. Lett.*, *189*(3-4), 103–114.

François, T., E. B. Burov, B. Meyer, and P. Agard (in press), Surface topography as key constraint on thermo-reological structure of cratons, *Tectonophysics*, doi:

644 10.1016/j.tecto.2012.10.009.

645 Frisch, W., and A. Al-Shanti (1977), Ophiolite belts and the collision of island arcs in the
646 Arabian Shield, *Tectonophysics*, *43*(3-4), 293–306.

647 Gao, S., P. Davis, H. Liu, P. Slack, Y. Zorin, N. Logatchev, M. Kogan, P. Burkholder,
648 and R. Meyer (1994), Asymmetric upwarp of the asthenosphere beneath the Baikal rift
649 zone, Siberia, *J. Geophys. Res.*, *99*, 15–319.

650 Geoffroy, L. (2005), Volcanic passive margins, *C. R. Géoscience*, *337*(16), 1395–1408.

651 Gerlings, J., K. Louden, and H. Jackson (2011), Crustal structure of the Flemish Cap Con-
652 tinental Margin (eastern Canada): an analysis of a seismic refraction profile, *Geophys.*
653 *J. Int.*, *185*(1), 30–48.

654 Gerya, T., L. Perchuk, and J. Burg (2008), Transient hot channels: perpetrating and
655 regurgitating ultrahigh-pressure, high-temperature crust-mantle associations in collision
656 belts, *Lithos*, *103*(1-2), 236–256.

657 Griffin, W., S. O'Reilly, J. Afonso, and G. Begg (2009), The composition and evolution
658 of lithospheric mantle: a re-evaluation and its tectonic implications, *J. Petrol.*, *50*(7),
659 1185.

660 Griffin, W. L., S. Y. O'Reilly, N. Abe, S. Aulbach, R. M. Davies, N. J. Pearson, B. J.
661 Doyle, and K. Kivi (2003), The origin and evolution of Archean lithospheric mantle,
662 *Precambrian Res.*, *127*, 19–41.

663 Hager, B., and M. Richards (1989), Long-wavelength variations in Earth's geoid: physical
664 models and dynamical implications, *Philos. T. Roy. Soc. A*, *328*, 309–327.

665 Hargrove, U., R. Stern, J. Kimura, W. Manton, and P. Johnson (2006), How juvenile is the
666 Arabian-Nubian Shield? Evidence from Nd isotopes and pre-Neoproterozoic inherited

667 zircon in the Bi'r Umq suture zone, Saudi Arabia, *Earth Planet. Sci. Lett.*, *252*(3-4),
668 308–326.

669 Henjes-Kunst, F., R. Altherr, and A. Baumann (1990), Evolution and composition of the
670 lithospheric mantle underneath the western Arabian peninsula: constraints from Sr- Nd
671 isotope systematics of mantle xenoliths, *Contrib. Mineral. Petrol.*, *105*(4), 460–472.

672 Hirth, G., and D. Kohlstedt (2003), Rheology of the upper mantle and the mantle wedge:
673 A view from the experimentalists, *Geophys. Monogr.*, *138*, 83–105.

674 Hofmann, A., and W. White (1982), Mantle plumes from ancient oceanic crust, *Earth*
675 *Planet. Sci. Lett.*, *57*(2), 421–436.

676 Huismans, R., and C. Beaumont (2011), Depth-dependent extension, two-stage breakup
677 and cratonic underplating at rifted margins, *Nature*, *473*(7345), 74–78.

678 Huismans, R. S., and C. Beaumont (2003), Symmetric and asymmetric lithospheric exten-
679 sion; relative effects of frictional-plastic and viscous strain softening, *J. Geophys. Res.*,
680 *108*(B10), 2496–2508.

681 Kaliwoda, M., R. Altherr, and H. Meyer (2007), Composition and thermal evolution of
682 the lithospheric mantle beneath the Harrat Uwayrid, eastern flank of the Red Sea rift
683 (Saudi Arabia), *Lithos*, *99*(1-2), 105–120.

684 Kameyama, M., D. Yuen, and S. Karato (1999), Thermal-mechanical effects of low-
685 temperature plasticity (the Peierls mechanism) on the deformation of a viscoelastic
686 shear zone, *Earth Planet. Sci. Lett.*, *168*(1-2), 159–172.

687 Kaus, B., J. Connolly, Y. Podladchikov, and S. Schmalholz (2005), Effect of mineral phase
688 transitions on sedimentary basin subsidence and uplift, *Earth Planet. Sci. Lett.*, *233*(1),
689 213–228.

690 Kuo, L., and E. Essene (1986), Petrology of spinel harzburgite xenoliths from the Kishb
691 Plateau, Saudi Arabia, *Contrib. Mineral. Petrol.*, *93*(3), 335–346.

692 Lavier, L., and G. Manatschal (2006), A mechanism to thin the continental lithosphere
693 at magma-poor margins, *Nature*, *440*(7082), 324–8.

694 Le Pourhiet, L. (2013), Strain Localization Due to Structural Softening During Pressure
695 Sensitive Rate Independent Yielding, *Bull. Soc. Geol. Fr.*, *184*(3).

696 Lenardic, A., and L. Moresi (1999), Some thoughts on the stability of cratonic lithosphere-
697 Effects of buoyancy and viscosity, *J. Geophys. Res.*, *104*(B6), 12,747–12,759.

698 Leroy, S., P. Gente, M. Fournier, E. d'Acremont, P. Patriat, M.-O. Beslier, N. Bellahsen,
699 M. Maia, A. Blais, J. Perrot, A. Al Kathiri, S. Merkouriev, J.-M. Fleury, P.-Y. Ruellan,
700 C. Lepvrier, and P. Huchon (2004), From rifting to spreading in the eastern Gulf of
701 Aden; a geophysical survey of a young oceanic basin from margin to margin, *Terra*
702 *Nova*, *16*(4), 185–192.

703 Leroy, S., F. Lucazeau, E. d'Acremont, L. Watremez, J. Autin, S. Rouzo, N. Bellahsen,
704 C. Tiberi, C. Ebinger, M.-O. Beslier, J. Perrot, P. Razin, F. Rolandone, H. Sloan,
705 G. Stuart, A. Al Lazki, K. Al-Toubi, F. Bache, A. Bonneville, B. Goutorbe, P. Huchon,
706 P. Unternehr, and K. Khanbari (2010a), Contrasted styles of rifting in the eastern Gulf
707 of Aden: A combined wide-angle, multichannel seismic, and heat flow survey, *Geochem.*
708 *Geophys. Geosyst.*, *11*, Q07,004.

709 Leroy, S., E. d'Acremont, C. Tiberi, C. Basuyau, J. Autin, F. Lucazeau, and H. Sloan
710 (2010b), Recent off-axis volcanism in the eastern Gulf of Aden: implications for plume-
711 ridge interaction, *Earth Planet. Sci. Lett.*, *293*, 140–153.

Leroy, S., P. Razin, J. Autin, F. c. Bache, E. d'Acremont, L. Watremez, J. Robinet, C. Baurion, Y. Denèle, N. Bellahsen, F. Lucazeau, F. Rolandone, S. Rouzo, J. Serra Kiel, C. Robin, F. c. Guillocheau, C. Tiberi, C. Basuyau, M.-O. Beslier, C. Ebinger, G. Stuart, A. Ahmed, K. Khanbari, I. Al-Ganad, P. de Clarens, P. Unternehr, K. Al-Toubi, and A. Al-Lazki (2012), From rifting to oceanic spreading in the Gulf of Aden: a synthesis, *Arab. J. Geosci.*, *5*(5), 859–901, doi:10.1007/s12517-011-0475-4.

Lithgow-Bertelloni, C., and P. G. Silver (1998), Dynamic topography, plate driving forces and the African superswell, *Nature*, *395*(6699), 269–272.

Little, T., M. Savage, and B. Tikoff (2002), Relationship between crustal finite strain and seismic anisotropy in the mantle, Pacific–Australia plate boundary zone, South Island, New Zealand, *Geophys. J. Int.*, *151*(1), 106–116.

Louden, K., J. Sibuet, and F. Harmegnies (1997), Variations in heat flow across the ocean-continent transition in the Iberia abyssal plain, *Earth Planet. Sci. Lett.*, *151*(3-4), 233–254.

Lucazeau, F., S. Leroy, A. Bonneville, B. Goutorbe, F. Rolandone, E. d'Acremont, L. Watremez, D. Düsünur, P. Tuchais, P. Huchon, N. Bellahsen, and K. Al-Toubi (2008), Persistent thermal activity at the Eastern Gulf of Aden after continental break-up, *Nat. Geosci.*, *1*, 854–858.

Lucazeau, F., S. Leroy, J. Autin, A. Bonneville, B. Goutorbe, L. Watremez, E. d'Acremont, D. Düsünur, F. Rolandone, and P. Huchon (2009), Post-rift volcanism and high heat-flow at the Ocean-Continent Transition of the Gulf of Aden, *Terra Nova*, *21*, 285–292.

734 Lucazeau, F., S. Leroy, F. Rolandone, E. d'Acremont, L. Watremez, A. Bonneville,
735 B. Goutorbe, and D. Düsünur (2010), Heat-flow and hydrothermal circulations at the
736 Ocean-Continent Transition of the Eastern Gulf of Aden., *Earth Planet. Sci. Lett.*, *295*,
737 554–570.

738 Manatschal, G. (2004), New models for evolution of magma-poor rifted margins based on
739 a review of data and concepts from West Iberia and the Alps, *Int. J. Earth Sci.*, *93*(3),
740 432–466.

741 McGuire, A. (1988), Petrology of mantle xenoliths from Harrat al Kishb: the mantle
742 beneath western Saudi Arabia, *J. Petrol.*, *29*(1), 73.

743 McKenzie, D., and M. Bickle (1988), The volume and composition of melt generated by
744 extension of the lithosphere, *J. Petrol.*, *29*(3), 625.

745 Minshull, T. (2002), Seismic Structure of the Oceanic Crust and Passive Continental
746 Margins, *International Handbook of Earthquake and Engineering Seismology*, *81A*, 911–
747 924.

748 Mjelde, R., T. Raum, Y. Murai, and T. Takanami (2007), Continent-ocean-transitions:
749 Review, and a new tectono-magmatic model of the Vøring Plateau, NE Atlantic, *J.*
750 *Geodyn.*, *43*(3), 374–392.

751 Molnar, P., H. Anderson, E. Audoine, D. Eberhart-Phillips, K. Gledhill, E. Klosko,
752 T. McEvilly, D. Okaya, M. Savage, T. Stern, et al. (1999), Continuous deformation
753 versus faulting through the continental lithosphere of New Zealand, *Science*, *286*(5439),
754 516–519.

755 Mooney, W., M. Gettings, H. Blank, and J. Healy (1985), Saudi Arabian seismic-refraction
756 profile: A traveltime interpretation of crustal and upper mantle structure, *Tectono-*

physics, *111*(3-4), 173–197.

Moulin, M., D. Aslanian, J. Olivet, I. Contrucci, L. Matias, L. Geli, F. Klingelhoefer, H. Nouze, J. Rehault, and P. Unternehr (2005), Geological constraints on the evolution of the Angolan margin based on reflection and refraction seismic data (ZaiAngo project), *Geophys. J. Int.*, *162*(3), 793–810.

Mutter, J., M. Talwani, and P. Stoffa (1982), Origin of seaward-dipping reflectors in oceanic crust off the Norwegian margin by "subaerial sea-floor spreading", *Geology*, *10*(7), 353–357.

Nasir, S., and A. Safarjalani (2000), Lithospheric petrology beneath the northern part of the Arabian Plate in Syria: evidence from xenoliths in alkali basalts, *J. Afr. Earth. Sci.*, *30*(1), 149–168.

ONeill, C., L. Moresi, D. Müller, R. Albert, and F. Dufour (2006), Ellipsis 3D: A particle-in-cell finite-element hybrid code for modelling mantle convection and lithospheric deformation, *Computers & geosciences*, *32*(10), 1769–1779.

Pasyanos, M., and A. Nyblade (2007), A top to bottom lithospheric study of Africa and Arabia, *Tectonophysics*, *444*(1-4), 27–44.

Pasyanos, M. E., and W. R. Walter (2002), Crust and upper-mantle structure of North Africa, Europe and the Middle East from inversion of surface waves, *Geophys. J. Int.*, *149*, 463–481.

Pérez-Gussinyé, M., and T. Reston (2001), Rheological evolution during extension at nonvolcanic rifted margins: Onset of serpentinization and development of detachments leading to continental breakup, *J. Geophys. Res.*, *106*(B3), 3961–3976.

779 Petit, C., and J. Déverchère (2006), Structure and evolution of the Baikal rift: a synthesis,
780 *Geochem. Geophys. Geosyst.*, *7*(11), Q11,016.
781 Poliakov, A., P. Cundall, Y. Podladchkov, and V. Lyakhovsky (1993), *Flow and Creep in*
782 *the Solar System: observations, modeling and theory*, chap. An explicit inertial method
783 for the simulation of viscoelastic flow: an evaluation of elastic effects on diapiric flow in
784 two-and three-layers models, pp. 175–195, Kluwer Academic Publishers.
785 Popov, A., and S. Sobolev (2008), SLIM3D: A tool for three-dimensional thermomechani-
786 cal modeling of lithospheric deformation with elasto-visco-plastic rheology, *Phys. Earth*
787 *Planet. In.*, *171*(1-4), 55–75.
788 Précigout, J., F. Gueydan, D. Gapais, C. Garrido, and A. Essaifi (2007), Strain localisation
789 in the subcontinental mantle – ductile alternative to the brittle mantle, *Tectonophysics*,
790 *445*(3-4), 318–336.
791 Ranalli, G. (1995), *Rheology of the Earth (2nd edit.)*, Chapman & Hall, London.
792 Ritsema, J., and H. van Heijst (2000), New seismic model of the upper mantle beneath
793 Africa, *Geology*, *28*(1), 63–66.
794 Saleeby, J., M. Ducea, and D. Clemens-Knott (2003), Production and loss of high-density
795 batholithic root, southern Sierra Nevada, California., *Tectonics*, *22*, 1064.
796 Sandvol, E., D. Seber, M. Barazangi, F. Vernon, J. Mellors Robert, and M. S. Al Amri Ab-
797 dullah (1998), Lithospheric seismic velocity discontinuities beneath the Arabian Shield,
798 *Geophys. Res. Lett.*, *25*(15), 2873–2876.
799 Sandwell, D., and W. Smith (1997), Marine gravity anomaly from Geosat and ERS 1
800 satellite altimetry, *J. Geophys. Res.*, *102*(10), 039–10.

Searle, M. (1983), Stratigraphy, structure and evolution of the Tibetan-Tethys zone in Zanskar and the Indus suture zone in the Ladakh Himalaya, *Trans. R. Soc. Edinburgh Earth Sci*, *73*, 205–219.

Shaw, J., J. Baker, A. Kent, K. Ibrahim, and M. Menzies (2007), The Geochemistry of the Arabian Lithospheric Mantle Source for Intraplate Volcanism?, *J. Petrol.*, *48*(8), 1495.

Sibuet, J. C., S. Srivastava, and G. Manatschal (2007), Exhumed mantle-forming transitional crust in the Newfoundland-Iberia rift and associated magnetic anomalies, *J. Geophys. Res.*, *112*(B6), 06,105.

Sobolev, A., A. Hofmann, D. Kuzmin, G. Yaxley, N. Arndt, S. Chung, L. Danyushevsky, T. Elliott, F. Frey, M. Garcia, et al. (2007), The amount of recycled crust in sources of mantle-derived melts, *Science*, *316*(5823), 412–417.

Sol, S., A. Meltzer, R. Bürgmann, R. Van der Hilst, R. King, Z. Chen, P. Koons, E. Lev, Y. Liu, P. Zeitler, et al. (2007), Geodynamics of the southeastern Tibetan Plateau from seismic anisotropy and geodesy, *Geology*, *35*(6), 563–566.

Song, T.-R. A., and D. Helmberger (2007), A depleted, destabilized continental lithosphere near the Rio Grande rift, *Earth and Planetary Science Letters*, *262*(1), 175–184.

Srivastava, S., and W. Roest (1995), Nature of Thin Crust Across the Southwest Greenland Margin and its Bearing on the Location of the Ocean-Continent Boundary, *Proceedings of the NATO-ARW Workshop on Rifted Ocean-Continent Boundaries, 11-14 May, 1994, Mallorca, Spain, Kluwer Academic, Dordrecht*, *1*, 95–120.

Stein, M., Z. Garfunkel, and E. Jagoutz (1993), Chronothermometry of peridotitic and pyroxenitic xenoliths: Implications for the thermal evolution of the Arabian lithosphere,

824 *Geochim. Cosmochim. Ac.*, *57*(6), 1325–1337.

825 Tiberi, C., S. Leroy, E. d'Acremont, N. Bellahsen, C. Ebinger, A. Al Lazki, and A. Pointu
826 (2007), Crustal geometry of the northeastern Gulf of Aden passive margin; localization
827 of the deformation inferred from receiver function analysis, *Geophys. J. Int.*, *168*(3),
828 1247–1260.

829 Turcotte, D., and G. Schubert (2002), *Geodynamics*, Cambridge University Press.

830 Unternehr, P., G. Pron-Pinvidic, G. Manatschal, and E. Sutra (2010), Hyper-extended
831 crust in the South Atlantic: in search of a model, *Pet. Geosci.*, *16*, 207–215, doi:
832 10.1144/SP369.10.

833 van Hunen, J., A. Van Den Berg, and N. Vlaar (2002), On the role of subducting oceanic
834 plateaus in the development of shallow flat subduction, *Tectonophysics*, *352*(3-4), 317–
835 333.

836 Van Wijk, J., and S. Cloetingh (2002), Basin migration caused by slow lithospheric ex-
837 tension, *Earth and Planetary Science Letters*, *198*(3), 275–288.

838 Van Wijk, J., J. Van Hunen, and S. Goes (2008), Small-scale convection during continental
839 rifting: Evidence from the Rio Grande rift, *Geology*, *36*(7), 575–578.

840 Vermeer, P. (1990), Orientation of shear bands in biaxial tests, *Geotechnique*, *40*(2), 223–
841 236.

842 Vigny, C., P. Huchon, J. Ruegg, K. Khanbari, and L. Asfaw (2006), Confirmation of
843 Arabia slow plate motion by new GPS data in Yemen, *J. Geophys. Res.*, *111*(B2),
844 B02,402.

845 Wallace, M., and D. Green (1991), The effect of bulk rock composition on the stabil-
846 ity of amphibole in the upper mantle: implications for solidus positions and mantle

847 metasomatism, *Miner. Petrol.*, *44*(1), 1–19.

848 Watremez, L., S. Leroy, S. Rouzo, E. d'Acremont, P. Unternehr, C. Ebinger, F. Lucazeau,
849 and A. Al Lazki (2011a), The crustal structure of the north eastern Gulf of Aden
850 continental margin: insights from wide angle seismic data, *Geophys. J. Int.*, *184*(2),
851 575–574.

852 Watremez, L., E. B. Burov, E. dAcremont, S. Leroy, and B. Huet (2011b), Mantle densities
853 and rupture criterion: thermo-mechanical modelling applied to the Eastern Gulf of
854 Aden, *Geophys. Res. Abstracts*, *Vol. 13*(33), EGU2011–9235.

855 Watts, A., and E. Burov (2003), Lithospheric strength and its relationship to the elastic
856 and seismogenic layer thickness, *Earth Planet. Sci. Lett.*, *213*(1-2), 113–131.

857 Wessel, P., and W. Smith (1995), New version of the Generic Mapping Tools released,
858 *Eos Trans. AGU*, *76*(33), 329.

859 White, R., and D. McKenzie (1989), Magmatism at Rifts zones: the generation of volcanic
860 continental margin and flood basalts, *J. Geophys. Res.*, *94*(1), 7685–7730.

861 Whitmarsh, R., P. Miles, L. Pinheiro, G. Boillot, and M. Recq (1991), The ocean-continent
862 transition of western Iberia, *Geobyte*, *75*(8), 1425.

863 Xu, W., C. Lithgow-Bertelloni, L. Stixrude, and J. Ritsema (2008), The effect of bulk
864 composition and temperature on mantle seismic structure, *Earth Planet. Sci. Lett.*,
865 *275*(1-2), 70–79.

866 Yamato, P., P. Agard, E. Burov, L. Le Pourhiet, L. Jolivet, and C. Tiberi (2007), Burial
867 and exhumation in a subduction wedge: Mutual constraints from thermomechanical
868 modeling and natural PTt data (Schistes Lustres, western Alps), *J. geophys. Res*, *112*,
869 B07,410.

Figure 1. Geodynamic settings of the Gulf of Aden.

Arrows show GPS vectors considering the Eurasian plate fixed [from *Vigny et al.*, 2006]; numbers are the velocities in mm/yr. Black dots are epicentres of earthquakes (USGS database from 1973/01 to 2011/04, $M_W \geq 3.5$ - http://earthquake.usgs.gov/earthquakes/ eqarchives/epic/). Hatched areas correspond to the Arabo-Nubian shield. Abbreviations: AFTZ, Alula-Fartak Transform Zone; AR, Aden Ridge; CR, Carlsberg Ridge; EAR: East African Rift; OFZ, Owen Fracture Zone; SHTZ, Socotra-Hadbeen Transform Zone; SR, Sheba Ridge; SSFZ, Shukra-el-Sheik Fracture Zone. The direction of extension of the Gulf of Aden is highlighted by the orientation of the transform zones. Relief is compiled from SRTM topography data [*Farr et al.*, 2007] and gravity-predicted bathymetry [*Sandwell and Smith*, 1997].

Figure 2. Model setup.

An extension velocity of 1 cm/yr is applied on each side of the model. The springs represent the lithostatic pressure (Winkler basement) that is applied at the base of the model. The strength envelopes (blue and red curves) compare the different rheological behaviour in depth for the two different mantle failure criteria in the upper 150 km of the model. The black curve presents the evolution of the temperature with depth in the upper 150 km of the model. A 50°C thermal anomaly is applied at the base of the crust to localize the deformation at the center of the model.

Figure 3. The Arabian plate mantle lithosphere buoyancy.

A. Composition of xenoliths from the Arabian plate mantle lithosphere (see Supplementary material for the references), of subcontinental mantle lithosphere standards from four tectons [*Griffin et al.*, 2009] and of the fertile Hawaiian pyrolite standard [*Wallace and Green*, 1991] plotted in a Mg# vs. $\%Al_2O_3$ diagram (Mg#=100 Mg/(Mg+Fe)). Also shown is the range of the tecton xenolith suites [*Griffin et al.*, 2009]. Two groups of xenoliths can be separated according to their chemistry. Lherzolites (lhz) and harzburgites (haz) have low Al_2O_3 content and high Mg#. In spite of the scattering, clinopyroxenites (cpx) and websterites (web) have high Al_2O_3 content and low Mg#.

B. Buoyancy calculated for the compositions of the xenoliths and the tecton standards along the initial thermal profile of the model (the buoyancy is calculated relative to the asthenosphere). The rapid buoyancy decrease between 50 km and 80 km shown by several curves of the cpx-web group corresponds to the plagioclase-spinel-garnet transitions.

C. Calculation of the Arabian plate mantle lithosphere buoyancy as a mixing of depleted and fertile rocks. The depleted fractions correspond to either the mean lhz-haz group (mean buoyancy $\sim$20 kg m^{-3}) or the mean of the tecton standards (mean buoyancy $\sim$5 kg m^{-3}). The fertile fraction corresponds to the cpx-web group (mean buoyancy $\sim$-100 kg m^{-3}). The buoyancy decreases with increasing fraction of cpx-web. The density of the "best fit model" (-20 kg m^{-3}, see section 5.1) can be achieved for a mantle lithosphere containing approximately 30% clinopyroxenite and websterite.

Figure 4. Influence of the mantle lithosphere rheology.

The two columns correspond to the results of the two models comparing mantle lithosphere rheology.

A. The first line shows the strain rate in the models 0.5 Ma before the break-up of the continental crust, respecting the color scale shown below. The second and third lines show the geometry of the model at the time of the break-up of the continental crust and 18 Ma later, respectively. The color code for the materials is the same as in Figure 2. The black arrows show the position of the oceanic spreading ridge.

B. Topography of the models at the moment of crustal break-up and 18 Ma afterwards compared with the present-day topography of the Gulf of Aden.

C. Evolution of the model topography through time: at each time line correspond a 2D topographic line. Left panel: Mohr-Coulomb model . Right panel: Perfectly-plastic model (following the columns of panel A). The higher elevations (dark red) show the positions of the rift shoulders through time while the narrow green-to-blue zone shows the position of the oceanic ridge. The black circles highlight the places where and times when the oceanic ridge relocates (ridge jumps). The black horizontal lines correspond to the moment of crustal break-up.

Figure 5. Influence of the mantle lithosphere buoyancy.

The three columns correspond to the results of the three models comparing the buoyancy of the lithosphere. Organization of this figure is similar to Figure 4.

Figure 6. Comparison with the eastern Gulf of Aden.

We compare available information with the model 18 Ma after crustal break-up.

A. Comparison of the heat-flow of the model with the heat-flow profile across the northern margin [*Lucazeau et al.*, 2008]. The blue dots are heat-flow values corrected for sedimentation, topography and refraction and the green line is the modeled heat-flow.

B. Comparison of the geometry of the model with a refraction and wide-angle reflection seismic profile coincident with the heat-flow measurements in part A of this figure [*Leroy et al.*, 2010a]. The grey box presents the geometry of the model and the possibility of partial melting in the mantle at the moment of crustal break-up. Z.E.C.M. means zone of exhumed continental mantle.

C. Comparison the model topography with data along 4 profiles [*Sandwell and Smith*, 1997; *Farr et al.*, 2007]. The positions of the profiles are shown on the map at the right of the figure. The red line corresponds to the position of the heat-flow/refraction line presented in A and B.

Table 1. Reference model parameters.

Parameters of the reference model having a Mohr-Coulomb failure criterion in the mantle lithosphere and equal densities in the mantle lithosphere and asthenosphere. Upper and lower crustal rheologies are dry granite and felsic granulite, respectively [*Ranalli*, 1995].

Parameters	Values			
Half extension velocity, V_{ext}	1×10^{-2} m yr^{-1}			
Temperature at the base of the lithosphere	1300 °C			
Radioactive heat production, H_s	4.5x10^{-10} W kg^{-1}			
Radiogenic production decay length, h_r	20 km			
Crust thermal conductivity, k_c	2.5 W K^{-1} m^{-1}			
Mantle thermal conductivity, k_m	3.3 W K^{-1} m^{-1}			
Specific heat, C_p	1000 J K^{-1} kg^{-1}			
Thermal age	700 Ma			
	Upper crust	Lower crust	Mantle lithosphere	Asthenosphere
Thickness (km)	24	20	206	
Density, ρ (kg m^{-3})	2750	2900	3330	3360
Initial scaling factor, A (Pa^{-n} s^{-1})	2.0×10^{-4}	8.0×10^{-3}	1.0×10^{4}	1.0×10^{4}
Power-law exponant, n	1.9	3.1	3.0	3.0
Activation energy, Q (J mol^{-1})	137×10^{3}	243×10^{3}	520×10^{3}	520×10^{3}
Cohesion, C_0 (MPa)	20	20	20	300
Internal angle of friction, ϕ (°)	30	30	30	2
Elastic shear modulus, G (Pa)	4.4×10^{10}	4.4×10^{10}	6.7×10^{10}	7.0×10^{10}

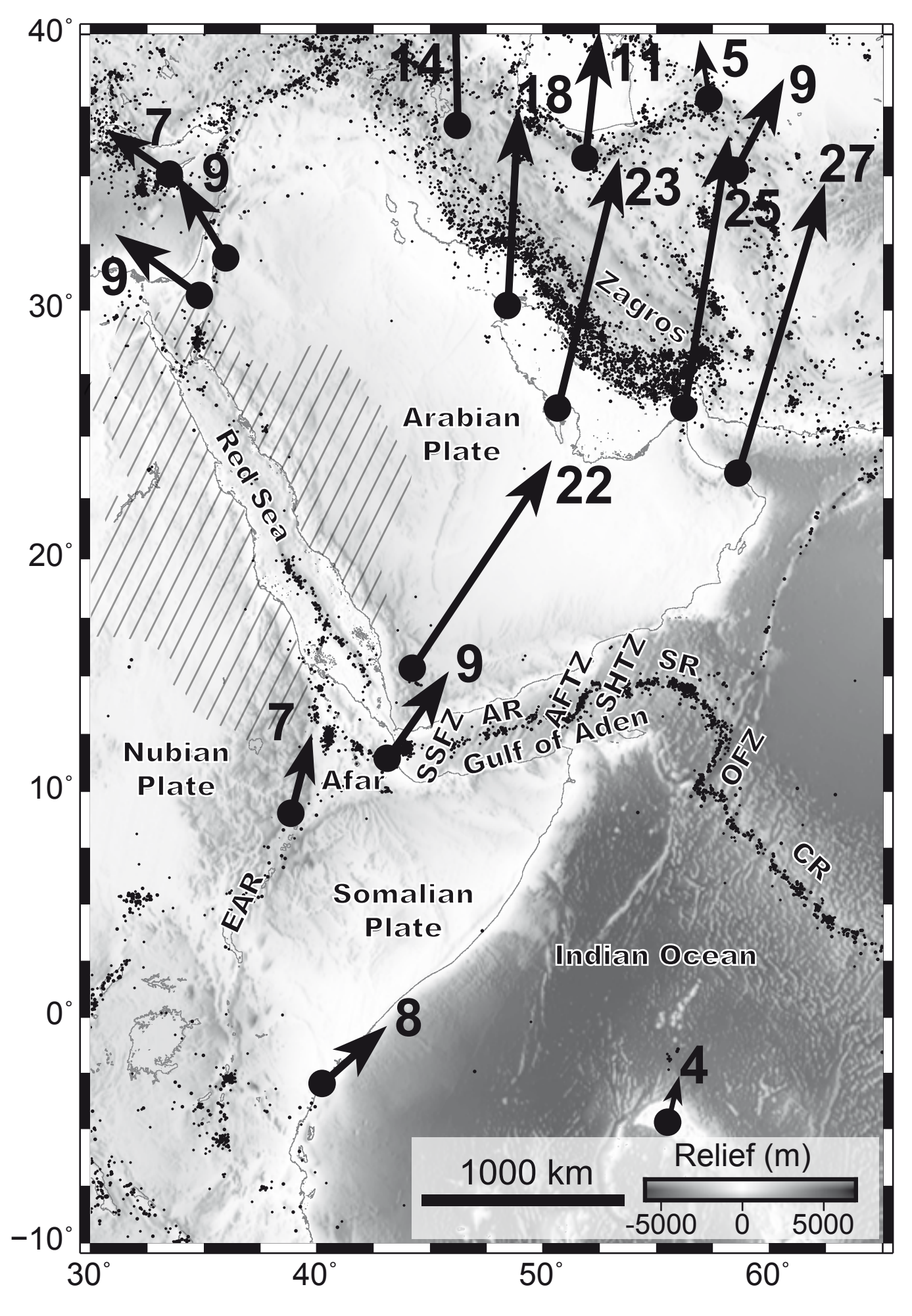
40°
30°
20°
10°
0°
−10°
30°
40°
50°
60°
14
18
11
5
9
7
9
23
25
27
9
Zagros
Arabian
Plate
Red Sea
22
9
7
SSFZ
AR
AFTZ
SHTZ
SR
Gulf of Aden
OFZ
CR
Nubian
Plate
Afar
EAR
Somalian
Plate
Indian Ocean
8
4
1000 km
Relief (m)
-5000
0
5000

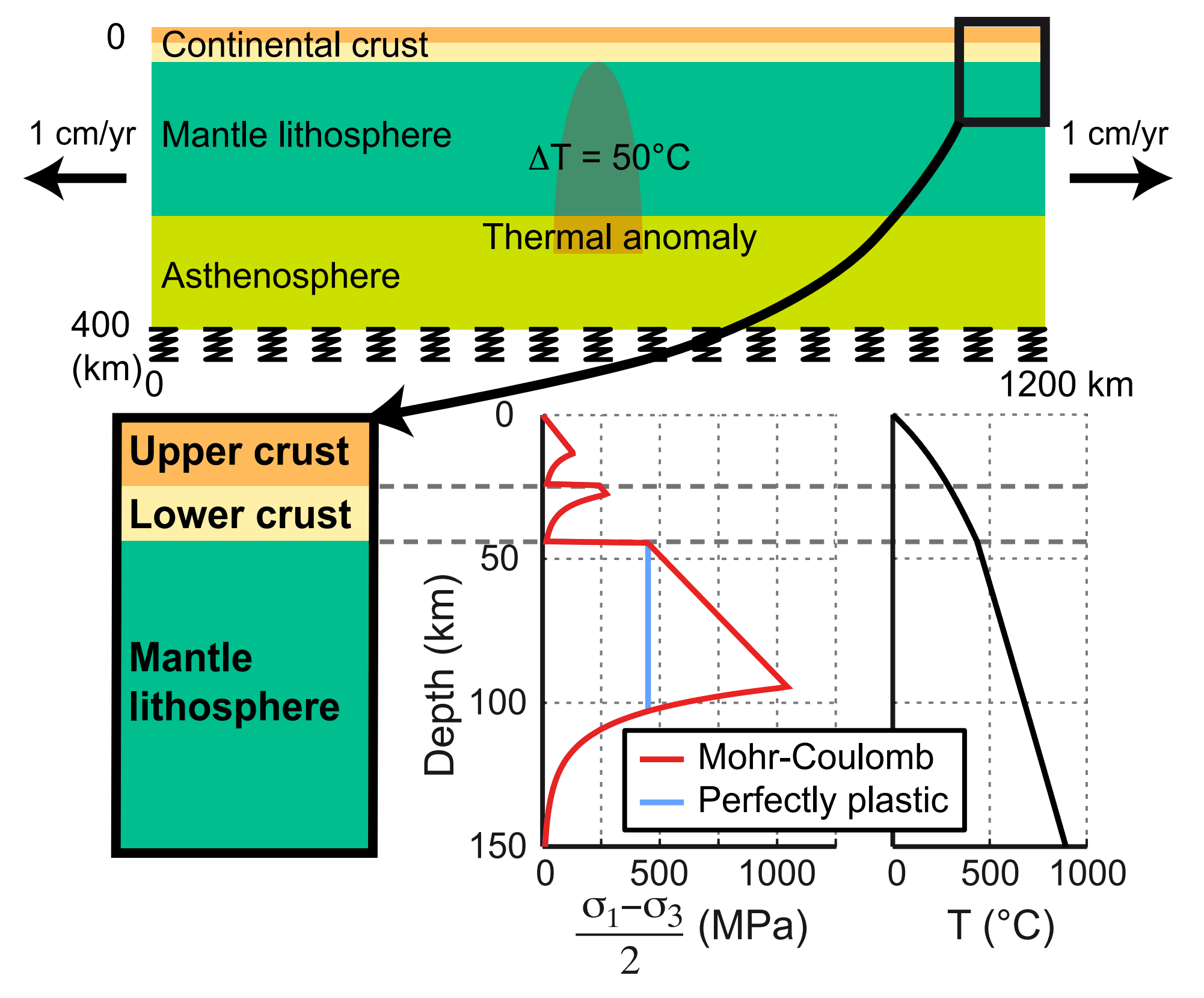
0
Continental crust
1 cm/yr
Mantle lithosphere
ΔT = 50°C
1 cm/yr
Thermal anomaly
Asthenosphere
400
(km)
0
1200 km
Upper crust
Lower crust
Mantle
lithosphere
0
50
100
150
Depth (km)
Mohr-Coulomb
Perfectly plastic
0
500
1000
σ1−σ3
2
(MPa)
0
500
1000
T (°C)

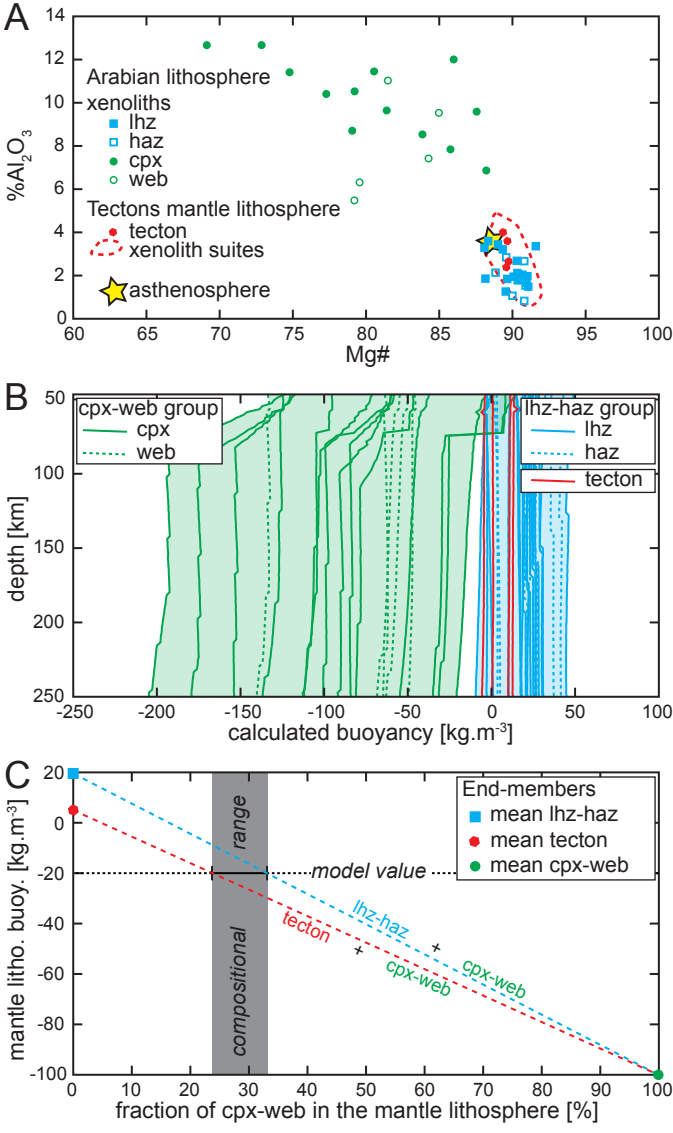
A
Arabian lithosphere
xenoliths
lhz
haz
cpx
web
Tectons mantle lithosphere
tecton
xenolith suites
asthenosphere
%Al2O3
Mg#
B
cpx-web group
cpx
web
lhz-haz group
lhz
haz
tecton
depth [km]
calculated buoyancy [kg.m-3]
C
End-members
mean lhz-haz
mean tecton
mean cpx-web
model value
range
compositional
lhz-haz
tecton
cpx-web
cpx-web
mantle litho. buoy. [kg.m-3]
fraction of cpx-web in the mantle lithosphere [%]

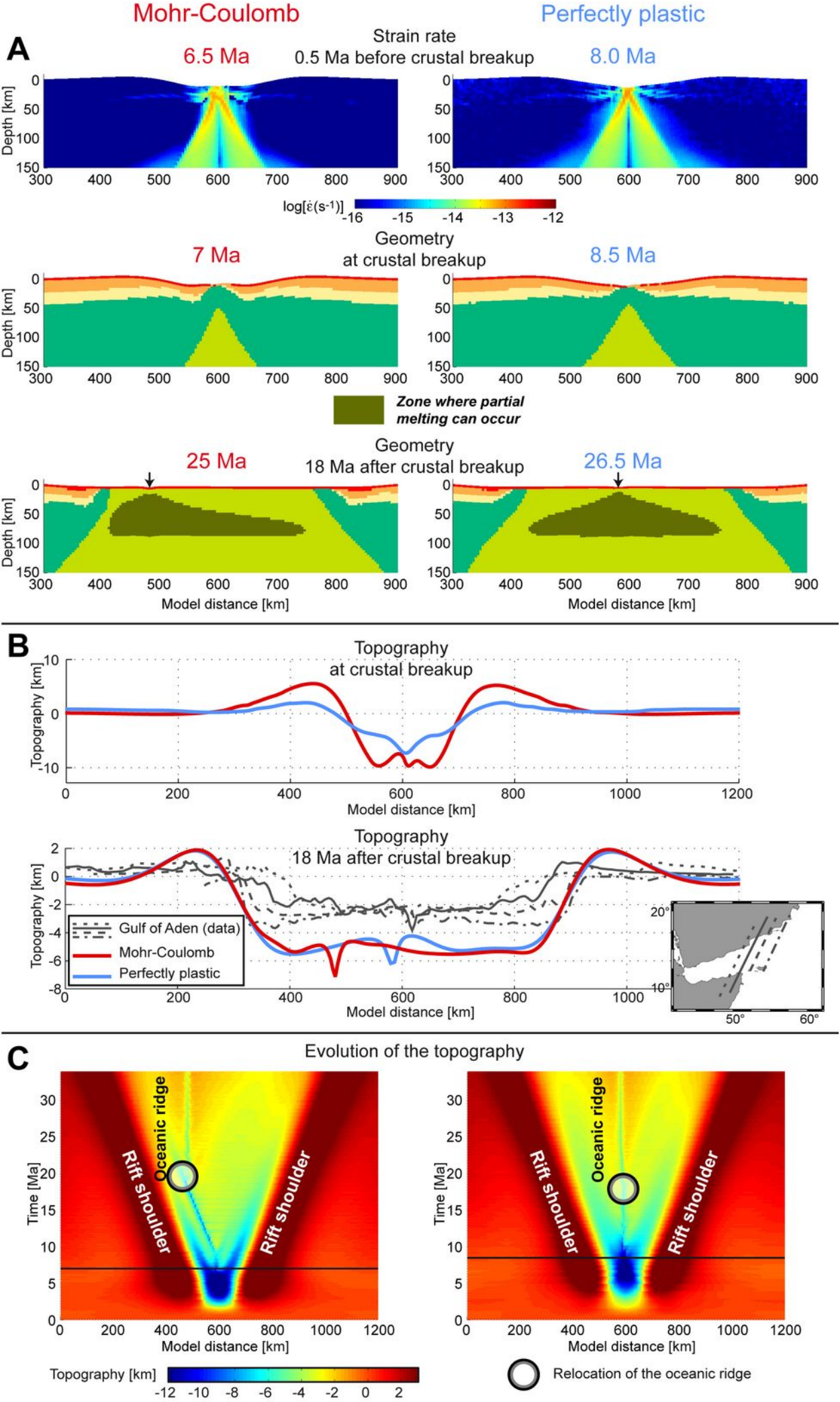
Mohr-Coulomb
Perfectly plastic
A
Strain rate
6.5 Ma
0.5 Ma before crustal breakup
8.0 Ma
Depth [km]
log[ε̇(s-1)]
-16 -15 -14 -13 -12
Geometry
at crustal breakup
7 Ma
8.5 Ma
Zone where partial melting can occur
Geometry
18 Ma after crustal breakup
25 Ma
26.5 Ma
Model distance [km]
B
Topography
at crustal breakup
Topography [km]
Topography
18 Ma after crustal breakup
Gulf of Aden (data)
Mohr-Coulomb
Perfectly plastic
C
Evolution of the topography
Oceanic ridge
Rift shoulder
Rift shoulder
Time [Ma]
Topography [km]
Relocation of the oceanic ridge

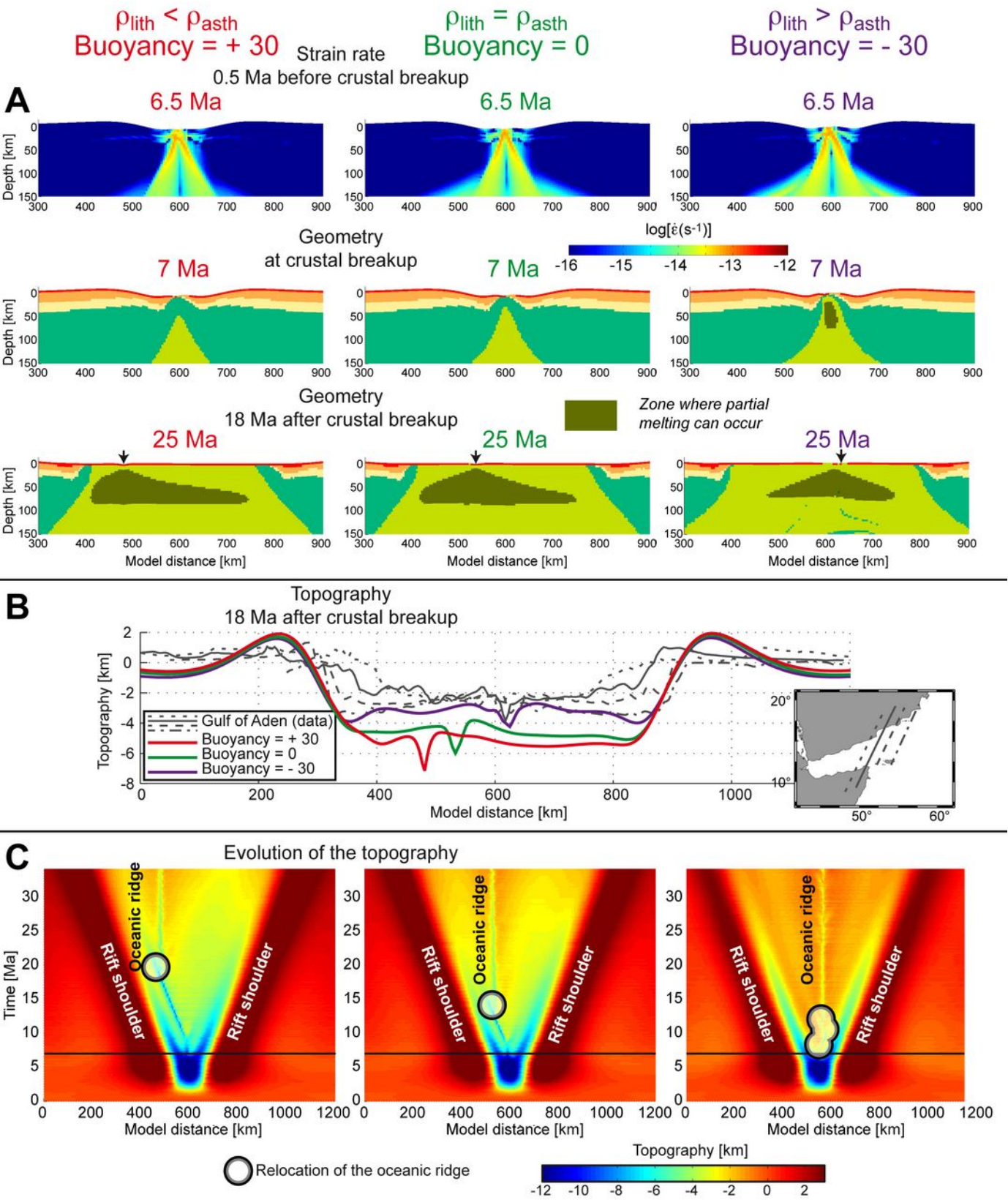
ρlith < ρasth
Buoyancy = + 30
ρlith = ρasth
Buoyancy = 0
ρlith > ρasth
Buoyancy = - 30
Strain rate
0.5 Ma before crustal breakup
A
6.5 Ma
6.5 Ma
6.5 Ma
Depth [km]
log[ε̇(s-1)]
-16 -15 -14 -13 -12
Geometry
at crustal breakup
7 Ma
7 Ma
7 Ma
Geometry
18 Ma after crustal breakup
Zone where partial melting can occur
25 Ma
25 Ma
25 Ma
Model distance [km]
B
Topography
18 Ma after crustal breakup
Topography [km]
Gulf of Aden (data)
Buoyancy = + 30
Buoyancy = 0
Buoyancy = - 30
Model distance [km]
20°
10°
50°
60°
C
Evolution of the topography
Time [Ma]
Oceanic ridge
Rift shoulder
Rift shoulder
Model distance [km]
Relocation of the oceanic ridge
Topography [km]
-12 -10 -8 -6 -4 -2 0 2

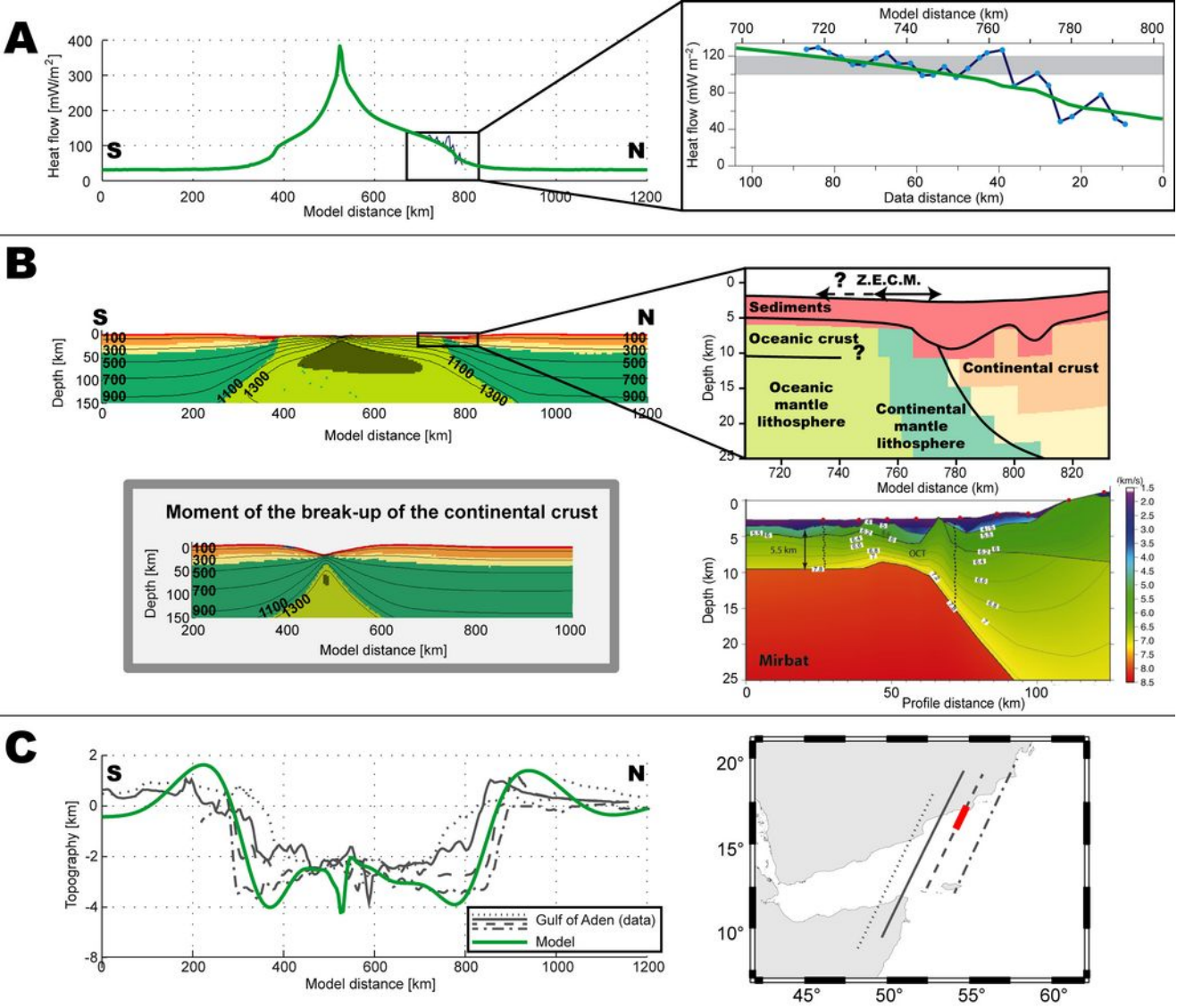
A
Heat flow [mW/m²]
S
N
Model distance [km]
Heat flow (mW m⁻²)
Data distance (km)
B
Depth [km]
Model distance [km]
? Z.E.C.M.
Sediments
Oceanic crust
Continental crust
Oceanic mantle lithosphere
Continental mantle lithosphere
Moment of the break-up of the continental crust
5.5 km
OCT
Mirbat
Profile distance (km)
(km/s)
C
Topography [km]
Gulf of Aden (data)
Model

Supplementary material

1 Density of the Arabian mantle lithosphere and asthenosphere

Bulk rock chemical analyzes of xenoliths from the mantle lithosphere below the Arabian shield have been gathered from literature [*Kuo and Essene*, 1986; *Nasir and Safarjalani*, 2000; *Stein et al.*, 1993; *Ghent et al.*, 1980; *Nasir*, 1992; *Nasir and Al-Fuqha*, 1988]. These xenoliths are found in neogene alkali basalts of Yemen, Saudi Arabia, Jordan, Israel and Syria [*McGuire*, 1988]. The dataset contains analyzes of lherzolites (N=16), harzburgites (N=7), clinopyroxenites (N=13) and websterites (N=5). The analyzes of the xenoliths as well as those of the fertile Hawaiian pyrolite and of four standard compositions of mantle lithosphere below tectons (lithospheres younger than 1 Ga) are presented in table 1. The densities corresponding to these chemical analyzes have been computed with the free energy minimization program PERPLEX07 [*Connolly*, 2009]. We used a thermodynamic database that is dedicated to mantle rocks thermodynamics [*Xu et al.*, 2008]. The activity model set takes into account solid solution in plagioclase, spinel, garnet, olivine, wadsleyite, clinopyroxene, orthopyroxene and high-pressure clinopyroxene (C2/C phase) in the six oxides Na_2O-CaO-FeO-MgO-Al_2O_3-SiO_2 system (NCFMAS). Even if the method is fairly similar, our results are not directly comparable to those of *Griffin et al.* [2009] who have not considered Na_2O in their computations. This assumption leads to higher density contrasts at depths below 400 km than with the six oxides system [*Nakagawa et al.*, 2010]. Chemical analyzes are generally given in the Na_2O-K_2O-CaO-FeO-MnO-MgO-Fe_2O_3-Al_2O_3-Cr_2O_3-TiO_2-SiO_2 eleven oxides system. Reduction from this whole system to the six oxides system has been carried out with the following assumptions. (1) The K molar amount, which is always minor, has been added to the Na molar amount. (2) The Mn molar amount, which is always minor, has been added to the Fe molar amount. (3) All iron is considered as Fe^{2+}. (4) Cr and Ti are assumed to be only present as oxides (chromite Cr_2O_3 and rutile TiO_2) and are therefore not considered. Amongst all tested assumptions, this set allows us avoiding large and probably unrealistic amount of excess Al_2O_3 and SiO_2 in the clinopyroxenites and the websterites. The density with depth for all the considered chemical compositions has been computed along the initial thermal profile of the models. These curves are presented on figure 1. Following *Nakagawa et al.* [2010], only buoyancy curves rather than absolute densities are presented in the text. We indeed consider that computing density differences reduces the uncertainties unavoidably arising from the chemical analyzes, the thermodynamic database and the activity models.

Table 1: Chemical compositions of the mantle lithosphere xenoliths from the Arabian shield, tectons mantle lithosphere [*Griffin et al.*, 2009] and asthenosphere (fertile Hawaiian pyrolite) [*Wallace and Green*, 1991]. The compositions are given in the reduced NCFMAS system, which has been considered for density computation with the free energy minimization program PERPLEX07 [*Connolly*, 2009]. Also given is the Mg# = 100 Mg/(Mg+Fe) relative to the compositions.References: 1: *Ghent et al.* [1980], 2: *Griffin et al.* [2009], 3: *Kuo and Essene* [1986], 4: *Nasir* [1992], 5: *Nasir and Al-Fuqha* [1988], 6: *Nasir and Safarjalani* [2000], 7: *Stein et al.* [1993], 8: *Wallace and Green* [1991].

Lherzolites								
Sample	M-1	K-3	T-5	A-4	R-9	JAR1	JAR3	JAR9
SiO_2	45.92	46.06	47.16	47.02	44.66	43.44	43.72	43.03
Al_2O_3	1.26	1.82	3.51	1.51	1.82	1.95	2.01	1.91
FeO	8.62	8.44	8.58	7.35	9.75	7.88	8.13	8.62
MgO	41.53	40.96	36.77	41.79	40.77	44.85	44.22	44.54
CaO	2.32	2.53	2.95	1.96	2.12	1.83	1.81	1.84
Na_2O	0.35	0.20	1.02	0.37	0.87	0.05	0.11	0.06
Mg#	0.90	0.90	0.88	0.91	0.88	0.91	0.91	0.90
Ref.	4	4	4	4	4	5	5	5
Sample	JAR15	JAR20	T6	B4	I1	TA-806	TA-842	MHZ-230
SiO_2	43.62	43.39	44.70	44.69	43.01	45.16	44.69	46.81
Al_2O_3	1.72	1.78	3.42	3.30	3.18	2.11	2.60	3.23
FeO	7.92	8.44	8.84	6.89	8.82	8.08	8.01	8.97
MgO	44.83	44.38	40.32	42.23	41.55	42.35	41.99	37.32
CaO	1.86	1.92	2.36	2.57	3.06	2.01	2.40	3.44
Na_2O	0.06	0.09	0.35	0.32	0.38	0.29	0.31	0.23
Mg#	0.91	0.90	0.89	0.92	0.89	0.90	0.90	0.88
Ref.	5	5	6	6	6	7	7	7
Harzburgites								
Sample	JT26A	JT26B	HAK-1	T3	B2	I3	H2	
SiO_2	44.70	45.05	44.25	42.85	44.32	43.54	42.24	
Al_2O_3	0.80	2.01	1.51	2.81	2.65	2.10	1.05	
FeO	8.19	8.19	7.98	9.02	7.90	9.57	9.15	
MgO	45.41	43.54	45.16	43.59	43.57	42.92	46.33	
CaO	0.80	1.01	0.92	1.46	1.40	1.70	1.17	
Na_2O	0.09	0.20	0.18	0.27	0.16	0.17	0.06	
Mg#	0.91	0.90	0.91	0.90	0.91	0.89	0.90	
Ref.	1	1	3	6	6	6	6	
Pyroxenites								
Sample	M-5	T-8	A-7	R-2	A-3	R-5	T1	T5
SiO_2	54.51	53.87	53.63	52.18	51.93	51.00	44.71	46.04
Al_2O_3	8.51	9.60	6.87	7.86	11.44	10.38	12.67	11.40
FeO	5.45	4.31	5.81	7.26	5.92	8.27	10.72	10.46
MgO	15.86	16.98	24.34	24.53	13.77	15.78	16.13	17.38
CaO	14.69	14.76	8.48	7.35	15.79	13.34	14.42	13.37

Continued on next page

Continued from previous page

Na_2O	0.98	0.48	0.87	0.82	1.15	1.23	1.36	1.34
Mg#	0.84	0.88	0.88	0.86	0.81	0.77	0.73	0.75
Ref.	4	4	4	4	4	4	6	6
Sample	B7	T8	I14	BS-701	KM-1402			
SiO_2	48.45	47.63	48.80	48.84	44.07			
Al_2O_3	8.69	9.64	10.53	12.01	12.65			
FeO	8.34	7.68	9.15	4.95	11.60			
MgO	17.65	18.86	19.57	17.02	14.55			
CaO	15.24	15.30	11.16	16.07	15.92			
Na_2O	1.62	0.89	0.78	1.10	1.21			
Mg#	0.79	0.81	0.79	0.86	0.69			
Ref.	6	6	6	7	7			
Websterites								
Sample	58376A	58376B	58377	T15	M11			
SiO_2	51.44	51.98	52.06	46.59	48.92			
Al_2O_3	7.39	6.29	5.48	11.03	9.52			
FeO	5.90	8.94	8.61	9.68	7.53			
MgO	17.72	19.49	18.37	23.87	23.89			
CaO	16.61	12.28	14.72	8.10	8.35			
Na_2O	0.93	1.02	0.77	0.73	1.78			
Mg#	0.84	0.80	0.79	0.81	0.85			
Ref.	1	1	1	6	6			
Asthenosphere								
Sample	Fert-Pyr							
SiO_2	45.80							
Al_2O_3	3.59							
FeO	8.74							
MgO	38.07							
CaO	3.13							
Na_2O	0.67							
Mg#	0.89							
Ref.	8							
Tecton mantle lithosphere								
Sample	Tc-1	Tc-2	Tc-3	Tc-4				
SiO_2	44.83	45.34	44.80	44.59				
Al_2O_3	3.53	3.93	2.62	2.33				
FeO	8.19	8.23	8.41	8.66				
MgO	40.09	38.99	41.47	41.95				
CaO	3.12	3.22	2.52	2.23				
Na_2O	0.24	0.28	0.18	0.24				
Mg#	0.90	0.89	0.90	0.90				
Ref.	2	2	2	2				

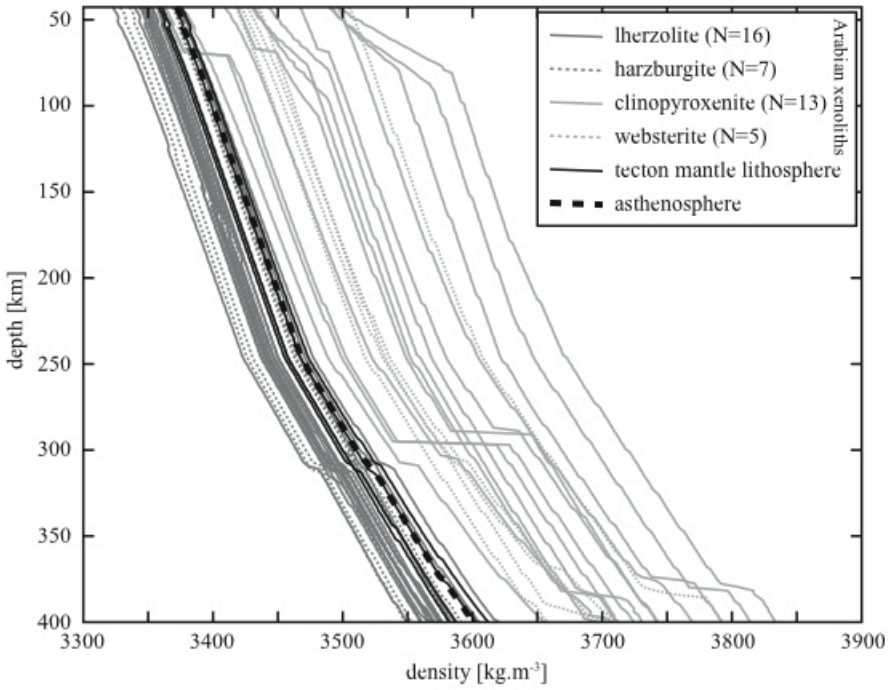

Figure 1: Density evolution with depth for mantle lithosphere xenoliths from the Arabian shield, tectons mantle lithosphere and asthenosphere. The computation of the density has been carried out with the free energy minimization program PERPLEX07 [*Connolly*, 2009].

References

Connolly, J. (2009), The geodynamic equation of state: what and how, *Geochem. Geophys. Geosyst.*, *10*, Q10,014.

Ghent, E., R. Coleman, and D. Hadley (1980), Ultramafic inclusions and host alkali olivine basalts of the southern coastal plain of the Red Sea, Saudi Arabia, *Am. J. Sci.*, *280-A*, 499–527.

Griffin, W., S. O'Reilly, J. Afonso, and G. Begg (2009), The composition and evolution of lithospheric mantle: a re-evaluation and its tectonic implications, *J. Petrol.*, *50*(7), 1185.

Kuo, L., and E. Essene (1986), Petrology of spinel harzburgite xenoliths from the Kishb Plateau, Saudi Arabia, *Contrib. Mineral. Petrol.*, *93*(3), 335–346.

McGuire, A. (1988), Petrology of mantle xenoliths from Harrat al Kishb: the mantle beneath western Saudi Arabia, *J. Petrol.*, *29*(1), 73.

Nakagawa, T., P. Tackley, F. Deschamps, and J. Connolly (2010), The influence of MORB and harzburgite composition on thermo-chemical mantle convection in a 3-D spherical shell with self-consistently calculated mineral physics, *Earth Planet. Sci. Lett.*, *296*(3), 403–412.

Nasir, S. (1992), The lithosphere beneath the northwestern part of the Arabian plate (Jordan): evidence from xenoliths and geophysics, *Tectonophysics*, *201*(3-4), 357–370.

Nasir, S., and H. Al-Fuqha (1988), Spinel-lherzolite xenoliths from the Aritain volcano, NE-Jordan, *Miner. Petrol.*, *38*(2), 127–137.

Nasir, S., and A. Safarjalani (2000), Lithospheric petrology beneath the northern part of the Arabian Plate in Syria: evidence from xenoliths in alkali basalts, *J. Afr. Earth. Sci.*, *30*(1), 149–168.

Stein, M., Z. Garfunkel, and E. Jagoutz (1993), Chronothermometry of peridotitic and pyroxenitic xenoliths: Implications for the thermal evolution of the Arabian lithosphere, *Geochim. Cosmochim. Ac.*, *57*(6), 1325–1337.

Wallace, M., and D. Green (1991), The effect of bulk rock composition on the stability of amphibole in the upper mantle: implications for solidus positions and mantle metasomatism, *Miner. Petrol.*, *44*(1), 1–19.

Xu, W., C. Lithgow-Bertelloni, L. Stixrude, and J. Ritsema (2008), The effect of bulk composition and temperature on mantle seismic structure, *Earth Planet. Sci. Lett.*, *275*(1-2), 70–79.